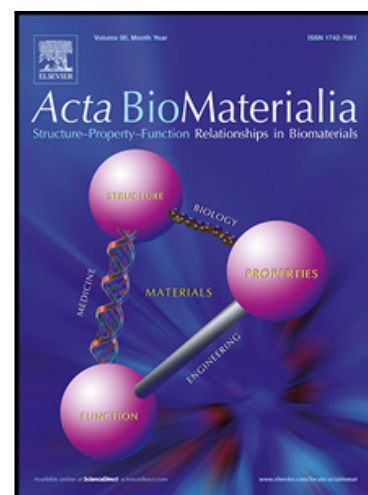# Journal Pre-proof

Multiscale Multimodal Characterization and Simulation of Structural Alterations in Failed Bioprosthetic Heart Valves

Elena Tsolaki , Pascal Corso , Robert Zboray , Jonathan Avaro , Christian Appel , Marianne Liebi , Sergio Bertazzo , Paul Philipp Heinisch , Thierry Carrel , Dominik Obrist , Inge K. Herrmann

Please cite this article as: Elena Tsolaki , Pascal Corso , Robert Zboray , Jonathan Avaro , Christian Appel , Marianne Liebi , Sergio Bertazzo , Paul Philipp Heinisch , Thierry Carrel , Dominik Obrist , Inge K. Herrmann , Multiscale Multimodal Characterization and Simulation of Structural Alterations in Failed Bioprosthetic Heart Valves, *Acta Biomaterialia* (2023), doi: https://doi.org/10.1016/j.actbio.2023.07.044

Multiscale Multimodal Characterization and Simulation of Structural Alterations in Failed Bioprosthetic Heart Valves

Elena Tsolaki[1,2,ˈ], *Pascal Corso*[3,ˈ], *Robert Zboray*[4], *Jonathan Avaro*[4], *Christian Appel*[5], *Marianne Liebi*[4,5,6],

Sergio Bertazzo[7,8], *Paul Philipp Heinisch*[9,10], *Thierry Carrel*[9,11]*, *Dominik Obrist*[3]*, *Inge K. Herrmann*[1,2,]*

[1]Laboratory for Particles-Biology Interactions, Department of Materials Meet Life, Swiss Federal Laboratories for Materials Science and Technology (Empa), Lerchenfeldstrasse 5, 9014 St. Gallen, Switzerland.
[2]Nanoparticle Systems Engineering Laboratory, Institute of Process Engineering, Department of Mechanical and Process Engineering, ETH Zurich, Sonneggstrasse 3, 8092 Zurich, Switzerland.
[3]ARTORG Center for Biomedical Engineering Research, University of Bern, Freiburgstrasse 3, 3010 Bern, Switzerland.
[4]Center for X-ray Analytics, Department of Materials Meet Life, Swiss Federal Laboratories for Materials Science and Technology (Empa), Ueberlandstrasse 129, 8600 Duebendorf, Switzerland.
[5]Paul Scherrer Institute, 5232 Villigen PSI, Switzerland
[6]Department of Physics, Chalmers University of Technology, 41296 Gothenburg, Sweden.
[7] Department of Medical Physics and Biomedical Engineering, University College London, WC1E 6BT, UK.
[8] London Centre for Nanotechnology, University College London, WC1E 6BT, UK.
[9] Department of Cardiovascular Surgery, Inselspital, University of Bern, Freiburgstrasse 18, Bern 3010, Switzerland
[10]Department of Congenital and Pediatric Heart Surgery, German Heart Center Munich, Technische Universität München, Germany.
[11] Department of Cardiac Surgery, University Hospital Zurich (USZ), Rämistrasse 101, 8091 Zürich, Switzerland
*thierry.carrel@usz.ch, *dominik.obrist@unibe.ch; *inge.herrmann@empa.ch; ingeh@ethz.ch
ˈE.T. and P.C contributed equally as first authors

Abstract

Calcific degeneration is the most frequent type of heart valve failure, with rising incidence due to the ageing population. The gold standard treatment to date is valve replacement. Unfortunately, calcification oftentimes re-occurs in bioprosthetic substitutes, with the governing processes remaining poorly understood. Here, we

present a multiscale, multimodal analysis of disturbances and extensive mineralisation of the collagen network in failed bioprosthetic bovine pericardium valve explants with full histoanatomical context. In addition to highly abundant mineralized collagen fibres and fibrils, calcified micron-sized particles previously discovered in native valves were also prevalent on the aortic as well as the ventricular surface of bioprosthetic valves. The two mineral types (fibres and particles) were detectable even in early-stage mineralisation, prior to any macroscopic calcification. Based on multiscale multimodal characterisation and high-fidelity simulations, we demonstrate that mineral occurrence coincides with regions exposed to high haemodynamic and biomechanical indicators. These insights obtained by multiscale analysis of failed bioprosthetic valves may serve as groundwork for the evidence-based development of more durable alternatives.

Keywords: Bioprosthetic valves, collagen mineralisation, calcification, calcium phosphate, multiscale characterisation

Introduction

Aortic valve stenosis is the most common valvular heart disease, affecting 12% of the population over the age of 75 [1, 2]. The disease involves fibrosis and deposition of calcium phosphate minerals on the valve leaflets, resulting in reduced leaflet movement, blood flow restriction, and other adverse outcomes, including angina and heart failure [3]. In moderate to severe aortic stenosis, valve replacement becomes inevitable, usually requiring open-heart surgery in younger and transcatheter techniques in older patients [4]. The valve is replaced either by a bioprosthetic (xenografts, allografts or exceptionally homografts) or a mechanical heart valve [4]. Unfortunately, subsequent calcification in bioprosthetic valves is frequently observed, limiting prosthesis durability significantly. Although mechanical valves overcome this drawback, they require lifelong anticoagulation therapy and put patients at risk of bleeding and thromboembolic complications [4]. Thus, they are primarily used in younger patients who do not qualify for bioprosthetic valves due to their limited durability.

Understanding the role and origin of calcification in native heart valves has been a major topic of research. Medical imaging studies using x-ray computer tomography and echocardiography have provided insights into the critical role of calcification in aortic valve stenosis, as increasing amounts of calcification correlate with disease severity in most patients [5, 6]. Studies have suggested that biomechanical stresses contribute to the development and progression of aortic valve stenosis [7-9]. For example, the earlier calcification onset observed in the non-coronary leaflet has been thought to be related to higher oscillatory shear stresses [7, 8]. In addition, considerable efforts by the molecular biology research community have focused on the mineralisation mechanisms in native valves, suggesting a complex, multifaceted process involving osteoblastic differentiation, downregulation of anti-calcific factors, mechanodynamics, shear stresses, chronic inflammation, as well as lipid accumulation [3, 10, 11].

Despite the growing mechanistic understanding of native heart valve calcification, it remains unclear whether similar mechanisms trigger the development of minerals in bioprosthetic valves. While some studies report shared aetiology [12], different cell types and protein contents associated with the mineral in native versus bioprosthetic valves have been reported [13, 14]. Calcification in bioprosthetic valves and subsequent failure have also been widely associated with the pretreatments used prior to implantation, i.e. tissue damages induced by preservation [3, 15, 16]. Recent research has indicated that calcification could result from an unmitigated immune response due to insufficient glutaraldehyde fixation (very low concentrations are usually used) [17]. Consequently, research on masking antigenicity through stronger fixation and decellularisation has been initiated [18, 19]. An overactive immune system is also believed to be the reason young patients undergoing bioprosthetic valve replacement are more prone to early calcification [20, 21]. Finally, the contribution of haemodynamic and biomechanical forces is debated, as it is suggested that areas experiencing higher haemodynamic and biomechanical stress are subject to higher incidents of structural alterations [22, 23]. Computational modelling investigations of the biomechanics and hemodynamics in calcified and non-calcified valves have been performed by various authors to gain further insights into the mechanism [24]. It is increasingly accepted that both transplant-related (residual donor cells and their debris [25], loss of glycosaminoglycans[25], and damage of collagen and/or elastin fibres during

chemical fixation and storage) and recipient-related (immune cell and red blood cell penetration, serum proteolytic enzymes, and calcium-binding proteins) factors promote dystrophic calcification of bioprosthetic heart valves [21].

Even though considerable advances have been made, bioprosthetic valvular failure remains a significant and unresolved issue (14). The apparent complexity of the mineralisation mechanisms has highlighted the need for a more in-depth, systematic understanding of the mineral structures present in bioprosthetic tissues. This is best illustrated by thorough electron microscopic investigations, which lead to significant advances in native valve calcification research, identifying distinct structures, including; calcified particles and compact calcification [2, 26, 27]. Similar structures have also been reported in explanted bioprosthetic valves; however, lacking histoanatomical context and high-resolution analysis [2, 28]. This disconnect between the clinicopathological investigations and the nanoanalytical findings obtainable by electron microscopy is prohibitive to a holistic understanding of bioprosthetic valve failure [21].

In this work, we combine clinically established methods such as (micro) computed tomography and histological analysis with cutting-edge material sciences methods, including scanning small angle x-ray scattering and electron microscopy, to provide comprehensive insights into mineralisation and structural changes in failed surgical bioprosthetic valve explants across scales. The findings are spatially correlated to macroscopic information on the biomechanical forces acting on the leaflets obtained through numerical simulations of the fluid-structure interaction between valve tissue and blood flow. Our analysis uncovers structural alterations in the collagen organisation associated with fibrillar mineralisation and provides a comprehensive characterisation of the minerals found in failed bioprosthetic valves with full histoanatomical context. Furthermore, it is shown that the spatial distribution of these minerals can be associated with regions exposed to complex blood flow patterns characterised by increased oscillatory shear index, topological shear variation index and residence time.

Materials and Methods

Sample collection

Failed bioprosthetic heart valves (Table S1) and native aortic valves (analysed as a reference) were kindly provided by the Department of Cardiovascular Surgery of the University Hospital Bern (Inselspital), Switzerland, following the obtainment of general written consent. All bioprosthetic valves were Perimount Magna Ease, tricuspid valves made of pretreated, fixed, bovine pericardium. Failed explanted valves were shipped in ethanol, post-fixed using 4% of paraformaldehyde (PFA) for 24 hours and then stored at 4 °C until further analysis. A new bioprosthetic valve (bovine pericardium Perimount Magna EASE 23 mm; stored in glutaraldehyde) was also obtained to serve as a control for the presence of minerals prior to implantation, and two old expired bioprosthetic bovine pericardium valves (Perimount Magna EASE 23 mm and 21 mm stored in glutaraldehyde) were used as a control for the induction of calcification during storage.

Micro X-ray computed tomography (CT)

For global microCT measurements, the valves were removed from PFA and placed in a saturated water atmosphere. The samples were mounted on a sample holder and scanned on a cone-beam RX Solutions Easy Tom XL microCT system, with a flat panel Varian PaxScan detector operated at an accelerating voltage of 140 kV with a tube current of 180 µA. The beam was pre-hardened using two copper filters (width: 0.7 mm) to reduce metal artefacts originating from the bioprosthetic valves' metal frame. All valves were scanned in the same manner. The voxel size of the microCT scans was around 20 µm. Manipulation of the data to further reduce metal artefacts (metal segmentation, histogram in-painting, and image fusion) was done using the RX solutions software. Following, leaflets of interest were cut out for higher resolution, local scans to be acquired. Valve leaflets were dissected using standard dissection tools and were placed in a saturated water atmosphere. High-resolution scans were obtained using an accelerating voltage of 75 kV and a tube current of 200 µA (for a global CT – voxel size ~ 14 µm) and 150 µA (for a local CT – voxel size ~ 3 µm). Prehardening of the beam was also performed using a 0.5 mm aluminium filter. The calcification percentage of individual leaflets from the micro-CT data was determined as a ratio of voxels belonging to the

calcification and those belonging to the calcification plus the leaflet tissue, obtained after segmentation of these structures. Adequate segmentation could be performed by gray value thresholding, due to the high contrast between those structures and the generally high image quality. Threshold gray values were typically 18 for background, 48 for leaflet tissue and 85 for calcifications on 8 bit gray scale. The 3D segmentation, rendering and analysis were done with VG Studio and FIJI ImageJ. For the cumulative spatial distribution of calcification, the images were registered using landmarks and transformed into binary text files where 1 corresponded to black (calcification) and 0 to white (tissue) and added up to evaluate the areas where most leaflets presented calcification.

Scanning electron microscopy

Regions of interest from isolated leaflets were identified based on the microCT data and were cut out using standard dissection tools for scanning electron microscopy (SEM). Samples were then dehydrated using an ethanol gradient of increasing concentrations, left to air dry, and mounted on silver stubs with carbon paste (Plano Leit C). The samples were silver painted and carbon-coated with 10 - 15 nm of carbon using a Safematic CCU-010 coater. An FEI Quanta 650 field emission gun environmental scanning electron microscope was used for imaging. Secondary electron (SE) and backscattered electron (BSE) signals were collected. Energy Dispersive X-ray (EDX) Spectroscopy analysis was carried out using the Thermo Fischer Pathfinder SDD EDX system. An accelerating voltage of 10 kV was used for all imaging and analysis. Size distribution analysis was carried out using FIJI ImageJ software. Box plots show interquartile (IQR) range and average values, and the whiskers indicate the minimum and maximum values.

Histology

A selection of isolated leaflets (based on the degree of calcification) was sent to SophistoLab, Muttenz, Switzerland, for paraffin embedding and sectioning. Sections were stained with hematoxylin and eosin (H&E) to observe the tissue architecture. The presence of calcification (appearing as brown/black) was examined through Von Kossa staining. The collagen network was also visualised through PicroSirius red

staining and polarised light microscopy, which enables the visualisation of the heterogeneity and organisation of collagen fibres. All images were recorded on a Zeiss AxioImager.Z2 using the brightfield or darkfield mode and the 5x, 20x objectives.

Confocal and two-photon microscopy

Collagen organisation and correlation with the mineral were evaluated using a Multi-Photon Leica SP8 MP microscope. Standard histological sections were used. The samples were incubated with a dilution of 1:10, near-infrared bisphosphonate-based calcium dye (OsteoSense 680, Perkin Elmer) for 20 minutes, washed with PBS and mounted using Fluoroshield mounting medium. The OsteoSense stained calcification was visualised using confocal imaging and collagen fibres through second harmonic generation imaging, using a MaiTai XF laser tuned at 880 nm and collecting the emission signal at 440 nm. Two internal and two external (a forward and a backward) detectors were used to capture the maximum collagen orientations. All images were captured using the 25x objective.

Small angle X-ray scattering

Scanning SAXS was performed at the cSAXS beamline at the Paul Scherrer Insitute with a monochromatic synchrotron-based x-ray beam focused to 25 x 25 μm^2 and a fixed-exit double Si(111) monochromators at an energy of 11.2 keV. 2D scattering patterns were recorded on a Pilatus 2M detector at two sample-detector distances, 7 m and 2 m, respectively, calibrated from the scattering pattern of silver behenate. The transmitted beam intensity was measured with a photodiode placed on the beamstop inside the steel flight tube under vacuum conditions. Bioprosthetic heart valves were measured in Kapton pockets filled with PBS buffer to maintain their hydration level. All three samples were raster-scanned at 100 x 100 μm^2 at a detector distance of 2 m to get an overview of the full leaflets. High-resolution scans for selected regions were performed at 50 x 50 μm^2 and a sample-detector distance of 7 m to complement the overview scans and assess potential changes in the collagen fibril diameter of non-implanted and explanted calcified heart valves. For the calcified sample, the selected region of 3 x 5 mm^2 contained a combination of calcified and

un-calcified tissues. A 1 x 1 mm^2 region was scanned for the non-implanted leaflet. Radial integration of 2D scattering patterns was performed following the azimuthal segment procedure using the cSAXS MatLab analysis package (Scanning SAXS Software Package, https://www.psi.ch/en/sls/csaxs/software (accessed: April 2018)). Radiation damage check was performed similarly for all samples prior 2D scans by monitoring a change of scattering when exposed to repeated 0.1 s exposure time over several seconds. The collagen fibril diameter was estimated by the peak maximal of background subtracted Gaussian fit of the fibrils in bundles' d-spacing peak between $0.02 < q < 0.09$ nm-1 (Fig. 5). Orientation analysis of collagen fibril diameter peak and tropocollagen 5th order of the diffraction peak stemming from the staggered supramolecular structure along the collagen fibre was also done. The 5th order peak was selected to avoid overlap with scattering from d-spacing of fibres in bundle (aka "collagen diameter") higher harmonics. A q-range selected between the 4th and 5th collagen peaks at $0.417 < q < 0.450$ nm^{-1} was selected to represent the orientation of the collagen or, when present, the mineral phases nanostructures (referred to as collagen/mineral q-equivalent domains (CMQED) within a size range of $13 < d < 37$ nm. Orientation analysis was performed on these regions following the analysis routine established by Bunk *et al.* 2009 [29]. The colour wheel contains information on the main orientation of nanoscale features (hue), their degree of orientation (saturation) and the amount of scattering material. With this encoding function, a material with a low electron density contrast will appear black, dense material with low preferential orientation will appear with a light colouration depending on the angle, and dense material with a strong preferential orientation will appear with vivid colours. Comparison of the three different scattering domains considered in this study, the d-spacing peak of collagen fibres in bundles, the 5th collagen peak and the CMQED allow us to probe, the average collagen bundles' main orientation, the average orientation of the tropocollagen molecules within a fibril, and the orientation of the mineral phases forming within the collagen structure respectively.

Coupled simulation of blood flow and leaflet dynamics

The computational method for the high-fidelity three-dimensional simulation of the blood mechanics and the solid dynamics of the biological aortic valve and aorta relied on a fluid-structure interaction (FSI)

approach based on a modified immersed boundary method [30]. The incompressible Navier-Stokes equation was solved on fixed staggered Cartesian grids (see blue domain in Fig. S17) of about 4 million cells using six-order compact finite differences; an explicit third-order Runge-Kutta time-stepping scheme for the advective term and a semi-implicit Crank-Nicolson scheme for the temporal discretisation of the diffusive term [31]. An iterative solution technique was developed to solve the large linear system of discretised equations for the fluid sub-problem. This technique was based on the Schur complement formulation and relied on the resolution of two Poisson problems on pressure solved with the Krylov subspace bi-conjugate gradient stabilised method (BiCGstab) with right preconditioning (geometric multigrid V(3,3)-cycle scheme as a preconditioner). A highly efficient commutation-based preconditioner matrix was indeed applied for the pressure iterations [31, 72]. A Helmholtz problem on velocity was also solved with the unpreconditioned BiCGstab method. The termination of the Helmholtz iterations and the convergence of the residuals in order for the continuity constraint to be met was controlled through an absolute threshold parameter $\varepsilon_U = 10^{-10}$ m/s or s^{-1} while the accuracy level in the Poisson iterations was dependent on the supremum norm of velocity divergence residuals between two consecutive iterates and a tolerance value set to 10^{-4} (31).

The elastodynamics equation was solved on a moving tetrahedral mesh consisting of about 200,000 tetrahedra constituted of 4 nodes each (see black and orange solids in Fig. S17) using the finite-element method with affine finite elements and a second-order central difference time-stepping scheme [32]. The Newton method was used to linearise the system of non-linear equations for the solid sub-problem and the linear system of equations was solved using a generalised minimal residual iterative method (GMRES) with an additive Schwarz preconditioner [32, 74]. The relative tolerance value to stop the iterations for the resolution of the linear and non-linear problems was set to 10^{-6} and 10^{-8}, respectively.

The same time step of 5 µs was imposed for both fluid and solid sub-problems that were then solved synchronously.

The strong coupling of these two sets of equations followed a segregated approach. This approach was based on a parallel variational transfer revolving around the resolution of a linear system built from L^2-projections equality and mortar integrals [73]. On the one hand, it allowed to project the fluid velocity to

the structural mesh to ensure the velocity equality at the fluid-structure interface. On the other hand, it allowed to transfer the reaction forces from the structural mesh to the fluid grid by adding a volumetric forcing term to the flow momentum equation ensuring the traction equality at the fluid-structure interface [33]. Moreover, an iterative procedure was implemented to ensure, by reaching a prescribed relative tolerance value of 10^{-6}, the velocity and forces equality at the fluid-structure interface [33]. Concerning the material properties for the structural parts of the studied FSI problem, a fibre-reinforced model was used to characterise the anisotropic material properties of the leaflets [34, 35], while the material properties of the aortic wall and the supporting crown of the leaflets are described by an isotropic linear elastic material model (density: 1500 kg/m^3 (crown); 1100 kg/m^3 (leaflets, aortic root and aorta), bulk modulus: 3 MPa and shear modulus: 0.3 MPa for all solid parts) [36]. The strain energy density function Ψ_{HGO} used to define the constitutive relation of the (non-calcified) leaflets modelled with a nearly incompressible anisotropic hyperelastic material was given by [34]:

$$\Psi_{\text{HGO}} = \frac{\mu_s}{2}(tr(\boldsymbol{C}) - 3) + \sum_{i=1}^{2}\frac{k_{1i}}{2k_{2i}}(\exp[k_{2i}(\boldsymbol{g}_i \cdot \boldsymbol{C}\boldsymbol{g}_i - 1)^2] - 1) + \frac{k_H}{2}(J - 1)^2, \qquad (1)$$

with μ_s, k_{1i}, k_{2i}, the fitted parameters of the model [35]; k_H, the penalty coefficient for the incompressibility constraint; J, the determinant of the deformation gradient tensor $\mathbf{F}$ (see Eq. (7)); $\boldsymbol{g}_i$, the fibre orientation (i.e. two families of collagen fibres oriented at a prescribed angle of 60° to each other) and $\mathbf{C}$, the right Cauchy-Green strain tensor (see definition in Eq. 7). Blood was approximated as an incompressible, homogeneous and Newtonian fluid [71] (density: 1060 kg/m^3, dynamic viscosity: 0.004 Pa.s).

The geometries of the bioprosthetic aortic valves created for the FSI simulations (Fig. S15 and Fig. S17) were inspired by the geometry of the commercial valve *Edwards Intuity Elite* (Edwards Lifescience, Irvine, CA, USA), which consists of three leaflets made from glutaraldehyde-pretreated bovine pericardium mounted on a rigid polymeric ring [37]. The geometry of the ascending aorta and aortic root was similar to that described in (36). It is worth noting that the considered geometry of sinus of Valsalva does not include coronary branches; hence no differentiation between right, left and non-coronary cusp for the nomenclature of the leaflet is provided. Two geometries of valve leaflets have been designed to highlight the influence of leaflet geometry on the predicted zones onto the leaflet surface where calcification would preferentially

occur. Moreover, these leaflet geometries have been chosen due to their unstable flutter motion noted in the FSI simulations throughout systole [36, 37].

The flow conditions considered in the computational study were peak systolic ones (i.e. only part of the whole cardiac cycle) under a pressure drop across the valves and in the ascending aorta of 8 mmHg over a time span of 0.3 s. The initial flow velocity over the fluid domain was set to zero and the initial leaflets' position is presented in Fig. S15 for both leaflet designs investigated in this computational study. The inflow conditions were imposed through the use of two to three cylindrical sponge layers (see green regions of Fig. S17), for which a forcing term was added to the flow momentum equation to prescribe a pressure gradient in the streamwise direction resulting in a pressure drop across the valves and in the ascending aorta of 8mmHg over a time span of 0.3 s. The evolution of the inflow rate was characterised by an initial acceleration phase from t=0 to t=0.1s, reaching a peak value of 16 L/min. Subsequently, there was a slight deceleration from t=0.1 to 0.18s, after which it remained constant at a value of 12 L/min until t=0.3s. Periodic boundary conditions were imposed at the borders of the Cartesian fluid grid. Finally, zero-displacement conditions are imposed at the nodes of the tetrahedral mesh located in the cross-sections at the extremity of the aorta model.

Indicators for the calcification characterisation from FSI simulations

The analysis of the flow field at the fluid-leaflet interface is based on blood-flow-related indicators found in the literature to trigger endothelial cell response at the vascular wall through biochemical signals leading to atherosclerotic lesions [38-41]. In this study, we hypothesise that, although these descriptors are commonly used to predict atheroprone regions resulting in changes in the vascular wall morphology, these indicators could also be valuable to macroscopically highlight zones prone to mineral nucleation and growth in bioprosthetic heart valves. A list of five indicators depending on the blood velocity close to the leaflet and their definition are provided below.

The wall shear stress vector in an incompressible flow of Newtonian fluid, which is defined as the projection of the viscous stress tensor (equivalent to the viscous shear stress tensor for incompressible flows) onto the leaflet wall normal vector is given by [40]:

$$\boldsymbol{WSS} = 2\mu\boldsymbol{S} \cdot \boldsymbol{n} \; [Pa], \tag{2}$$

with **S,** the strain-rate tensor of the local fluid element, **n**, the normalised vector normal to the leaflet wall and $\mu = 0.004$ Pa.s, the dynamic viscosity of blood. To ensure that no spurious normal stresses are taken into account to compute the WSS vector, the diagonal elements of the rate-of-strain tensor **S** have been set to zero.

The wall shear stress vector is the quantity based on which the other indicators are computed in the rest of this paper, and the time-averaged value of its magnitude (TAWSS) corresponds to one indicator used in the present study. The time-averaged pressure (TAP) represents the diagonal part of the total stress (the fluid exerts onto the leaflet surface) tensor.

The oscillatory shear index (OSI)) is used to quantify the temporal variability of the wall shear stress vector and is defined as [39]:

$$OSI = \frac{1}{2}\left[1 - \frac{\| \int_0^T \boldsymbol{WSS} \, dt \|}{\int_0^T \| \boldsymbol{WSS} \| \, dt}\right], \tag{3}$$

With $\|\boldsymbol{WSS}\|$, the L^2-norm of the wall shear stress vector and T, the simulated time over peak systole.

The relative residence time (RRT, multiplied by the constant dynamic viscosity to obtain a RRT expressed in seconds) [38, 39] is calculated from the TAWSS and OSI indicators as follows:

$$RRT = \mu \frac{1}{(1 - 2\, OSI)TAWSS} \; [s], \tag{4}$$

The topological shear variation index (TSVI) as proposed in [38, 42] is considered in this study as an indicator to represent the expansion and contraction at the leaflet surface due to the spatial variation of the wall shear stress vector and calculated by taking the root mean square of the instantaneous temporal fluctuations of the wall shear stress divergence over the systolic phase. This is thus calculated with the following equation:

$$TSVI = \sqrt{\frac{1}{T} \int_0^T (\nabla \cdot WSS_u - \overline{\nabla \cdot WSS_u})^2 \, dt} \ [m^{-1}], \qquad (5)$$

with $\nabla \cdot$, the divergence operator, $\overline{o}$, time-averaging operation and $\boldsymbol{WSS_u}$, the wall shear stress unit vector

$= \frac{\boldsymbol{WSS}}{\|\boldsymbol{WSS}\|}$.

In order to characterise from the computational fluid-structure analyses the mechanics of the leaflets and the influence thereof on the fibre damage in the tissue-based bioprosthesis, two additional indicators pertaining to the leaflet dynamics are computed. The first one is the time-averaged von Mises stress, which is dependent on the symmetric Cauchy stress tensor σ:

$$\sigma_{vM} = \sqrt{\frac{1}{2} [(\sigma_{11} - \sigma_{22})^2 + (\sigma_{22} - \sigma_{33})^2 + (\sigma_{33} - \sigma_{11})^2 + 6(\sigma_{23}^2 + \sigma_{31}^2 + \sigma_{12}^2)]} \ [Pa]. \qquad (6)$$

The second indicator is the time-averaged scalar strain defined as the trace of the right Cauchy-Green strain tensor **C**:

$$SS = tr(\boldsymbol{F^T F}) \ [-], \qquad (7)$$

With $\mathbf{F} = \nabla_x \boldsymbol{u}_s + \mathbf{I}$, the deformation gradient tensor; **u_s**, the displacement vector of the leaflet from the initial configuration and **I**, the identity tensor.

Equation for the reconstructed calcification intensity field

In order to reconstruct a calcification-prone intensity field that depends on the aforementioned indicators, a procedure has been established. Similarly to the approach presented in Corso *et al.* [43] for establishing fitted models for the evaluation of pressure gradient and haemodynamic stresses, this procedure relies on a non-linear least-square minimisation problem. The non-linear function for which the coefficients need to be fitted can be expressed as follows:

$$f_{calcI^{recon}} = C_1 TSVI_{d,Ao}^{C_2} + C_3 TAWSS_{d,Ven}^{C_4} + C_5 SS_{d,Ao}^{C_6}, \qquad (8)$$

with C_i, the coefficients to be fitted (with i ranging from 1 to 6). The coefficients of the exponents are set to be positive. The choice of the three indicators (namely TSVI on the aortic side of the leaflets and TAWSS on the ventricular side of the leaflets and motion-based SS on the aortic side) for the minimisation procedure

stems from quantitative data observed in the results for each individual indicator (see Figure 6), in line with the spatial distribution of the microCT reference data. It is worth noting that, for the least-square fitting procedure, the chosen indicators' values as well as the calcification intensity field obtained from microCT images are first normalised so that the range of values for each indicator varies from 0 to 1. In addition, the values of the normalised indicators and reference calcification intensity were distributed over bins of 0.005 and then normalised so that the integral over the discrete distributions is equal to one. The normalised distribution of each indicator is referenced with the subscript "d" in Eq. 8. The distribution of the reference calcification intensity observed from the microCT measurements is referred to as $calc\mathbf{I}^{ref}$ (cf. Fig. 1C) and the objective function of the minimisation problem using the least-square method is equal to $\left\| f_{calcI}^{recon} - calc\mathbf{I}^{ref} \right\|_2^2$. The training and prediction accuracy was assessed by calculating the coefficient of determination R^2, which represents the proportion (as a percentage of the variance of the observed data) of the prediction that agrees with the observed data. To do so, the data consisting of the distribution data for the three indicators at the leaflets' aortic or ventricular surface and the reference calcification intensity data (observed data) were split into a training and testing sets of 100 bins each (see Fig. 7A and 7B). The prediction accuracy thus quantifies the level of concurrence between the distribution of the normalised indicators and the reference calcification intensity over bins that differ from those used in the training dataset. That is to say, the distributions over the two bin sets correspond to the distributions of the indicators values and reference calcification intensity over different points taken onto the leaflets. Therefore, the prediction accuracy served as a metric for assessing the model's ability to predict the distribution of calcification from the indicators based on points located on the leaflets that differed from those used for the model training, while utilising the same reference calcification intensity data.

Statistical analysis

Origin Pro 2020b software (OriginLabs, Massachusetts, USA) was used for all statistical analyses. Linear regression fitting was carried out to evaluate the relationship between implantation duration and

calcification area percentage and maximum calcification thickness (N=21 (all explanted leaflets obtained)) and between maximum thickness and the calcification area percentage (n=14 (all macroscopically calcified leaflets as identified by CT data)). The results are reported using the Pearson's correlation coefficient (r). The mineral dimension data was plotted in boxplots as the interquartile range (IQR) with whiskers representing the minimum and maximum values, and individual data points included as rhombic points.

Results and Discussion

Macroscale structural assessment shows calcification of the leaflet belly

To assess the presence, amount, and anatomical location of calcification in failed explanted surgical bovine pericardium bioprosthetic valve leaflets (Fig. 1A) at the macroscale, microCT scanning and reconstruction were performed. The twenty-one valve leaflets (isolated from seven explanted heart valves from 3 female and 4 male patients) analysed by CT, contained a variable degree of macroscopic calcification (non-calcified (n=7), calcified (n=14), see Table S1). There was a trend that valves explanted from female patients (3 out of 9 leaflets calcified, 1 out of 3 valves explanted due to calcification) were less calfified than those from male patients (11 out of 12 leaflets calcified, 4 out of 4 valves explanted due to calcification). It was observed that in highly calcified leaflets, the mineral covered the entire belly area affecting the free edge and the commissures (Fig. 1B). In moderately calcified leaflets, the mineral was present in irregular patterns spreading from the lower and central parts of the belly near the annulus to the commissures, with the free edge remaining largely unaffected (Fig. 1B). A similar pattern was observed in the least calcified leaflets with commissures and free edge largely calcification-free (Fig. 1B).
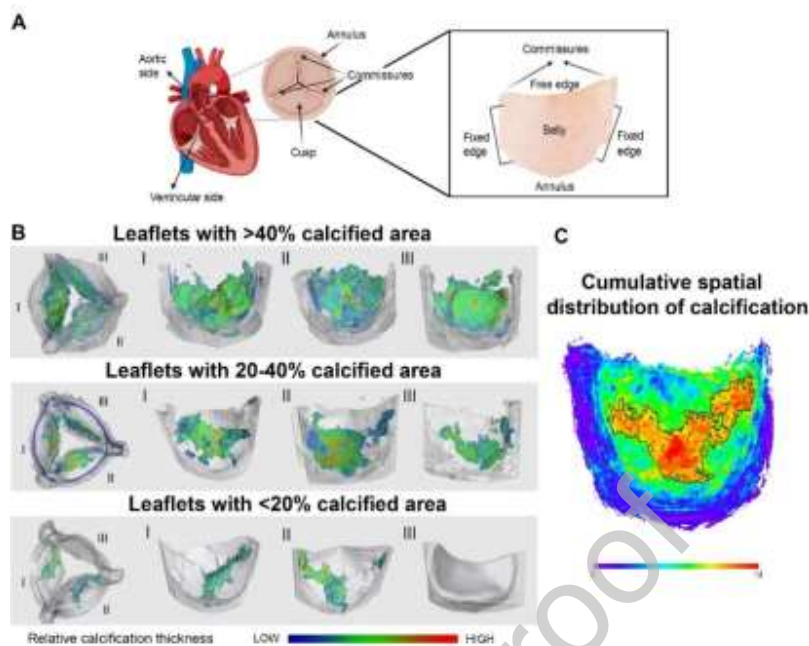
Fig. 1. Macroscale anatomical analysis of calcification in bioprosthetic valves. (A) *Schematic diagram of a tricuspid aortic valve as viewed from the aortic side and individual isolated cusp with the aortic side shown for reference.* ***(B)*** *Representative global microCT of calcified bioprosthetic valves, and* ***I***, ***II*** *and* ***III*** *corresponding higher magnification global microCT of individual valvular leaflets presenting different calcification degrees.* ***(C)*** *Heatmap of the relative cumulative spatial distribution of calcification using all calcified leaflets (n=14) where purple (intensity 0) and blue correspond to non-calcified areas and red (intensity 14) corresponds to calcified areas observed in all leaflets, indicating that the central parts of the leaflet belly (black outline) was calcified in most (orange areas) or all (red areas) leaflets. Shapes aligned to outer leaflet dimensions.*

Interestingly, the calcification patterns in the different leaflets indicate that the region most commonly calcified is the central area of the leaflet belly (Fig. 1C, region indicated by black outline) with the area appearing as saturated red (corresponding to intensity value 14) being calcified in all leaflets containing microCT-detectable minerals. This data could indicate a progressive process where calcification occurs initially in the lower and central parts of the belly and extends gradually to the entire leaflet. The presence of a progressive process is further supported by strong correlations (Pearson's $r > 0.89$) between the amount of leaflet calcification and maximum mineral thickness (growing up to 1.33 mm) with the duration of implantation (Fig. S1). However, despite the observed trend of mineral accumulation in the central part of the belly, the variation in mineral patterns in the peripheral regions varies significantly, possibly due to a complex, multifaceted formation mechanism.

Micro and nanoscale characterisation reveals the presence of mineralised collagen fibrils

For more detailed information on the mineral structures, high-resolution microCT reconstructions (voxel size of 3 µm) of individual leaflets were carried out, revealing the presence of fibrous structures (Fig. 2A and S2) along with regions of compact calcification (Fig. 2A III top and bottom). Calcified regions were microdissected from the belly of nine macroscopically calcified leaflets isolated from seven valves and characterised by high-resolution SEM (Fig. 2B). The highly abundant calcified fibres exhibited diameters between 0.5 – 6.4 µm (average: 1.8 µm, IQR: 0.9 µm), were partially formed by organic material based on electron density (Fig. 2B, C and S3) and were observed in all macroscopically calcified leaflets analysed by SEM. Interestingly, these large calcified fibres were formed by bundles of smaller calcified fibrils (average: 109 nm, IQR: 53 nm) (Fig. 2B, C and S3) aligned to some extent along the same axis. Their characteristic diameters match the diameters of collagen type I fibrils (10 - 500 nm in diameter, also observed through SAXS measurements, *vide infra*) and fibres (1 - 20 µm in diameter) [44, 45], thus supporting the widely accepted collagen mineralization theory described for native valves [46]. These mineralised fibre and fibril structures were not detected in the native heart valves investigated by us (Fig. S4) nor in previous electron microscopy studies [2, 26, 27].
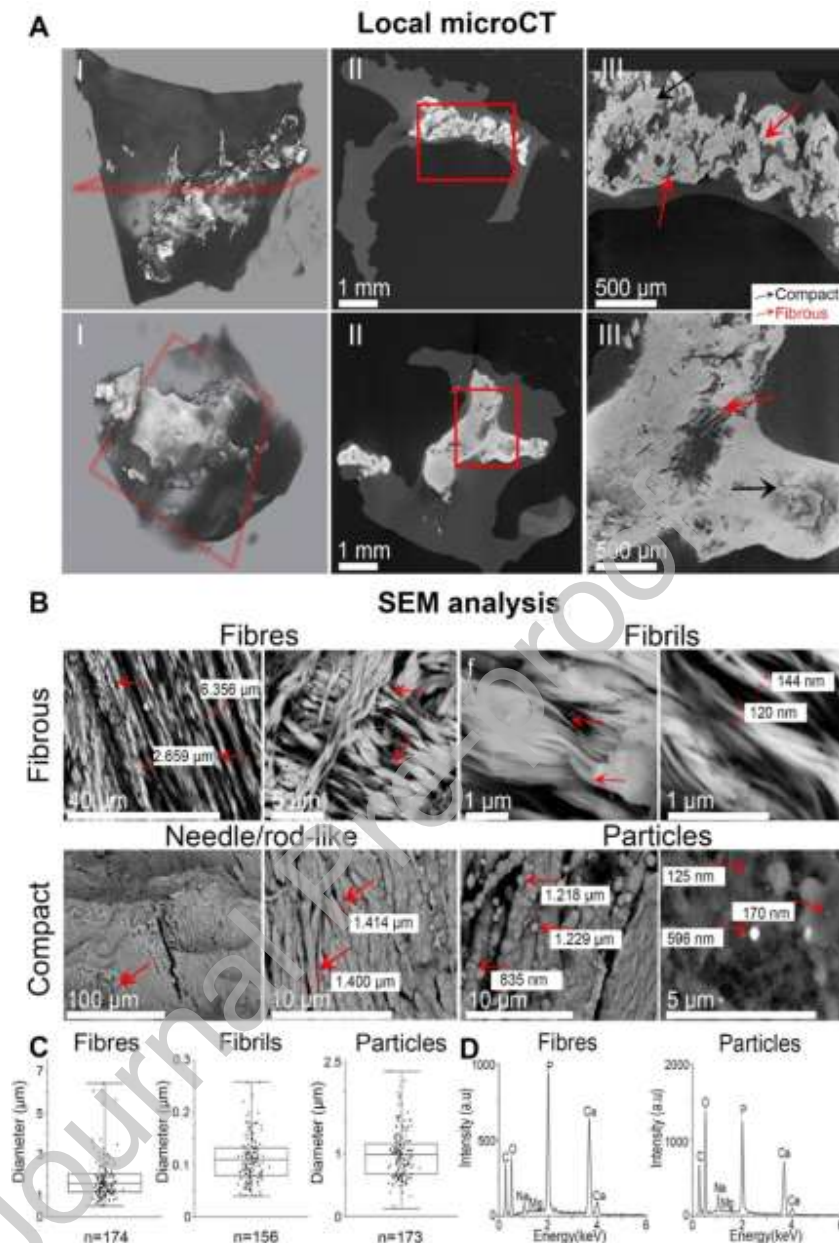
Fig. 2. High-resolution imaging of minerals within macroscopically calcified bioprosthetic cusp tissue. *Inorganic material is shown as white/light grey and organic material as dark grey/black. (**A**) **I**, Representative high-resolution microCT reconstructions of valve leaflets with different calcification percentages, 16% and 33% (top and bottom row respectively) and **II**, cross-sections (indicated as a red rectangle in **I**) of the leaflets showing the calcification shape and **III**, higher magnification microCT images showing fibrous and compact regions. (**B**) Representative high-resolution BSE micrographs of fibrous regions show calcified fibres and fibrils (arrows) and compact regions formed by highly calcified fibres, needle/rod-like structures and calcified particles (arrows) observed in macroscopically calcified leaflets. Some individual calcified particles (arrows) were observed in less calcified areas. (**C**) Fibre (n=174), fibril (n=156) and particle (n=173) diameter size distributions. (**D**) Representative EDX spectra of calcified fibres and particles obtained from macroscopically calcified leaflets.*

More recently, Gourgas *et al.* [47] also reported fibrous structures that appear (partially) mineralized in native human heart valves, however, with seemingly low abundance and of unknown origin. Extensively calcified merged fibres were also occasionally detected within the more compact mineral structures observed (Fig. 2B), resembling calcified rods and needle-like crystals (Fig. 2B and S3). Additionally, calcified particles (average diameter: 1.0 µm, IQR: 0.5 µm) were detected in all macroscopically calcified leaflet samples (Fig. 2B-D and 4D). These particles often appeared aggregated in highly calcified regions, sometimes forming larger pearl-string structures (Fig. 2B and S3) and were also detected as individual entities in tissue parts where large calcifications were absent (Fig. 2B and S3). Similar particles have also been identified in native valves (Fig. S4), well in line with earlier works [2, 26, 27]. Based on EDX analysis, all minerals observed in highly calcified regions were formed by calcium phosphate and contained magnesium in some cases (Fig. 2D and S5).

To distinguish between superficial and deep-lying materials and their characteristics, regions from the aortic and ventricular surfaces of the nine macroscopically calcified leaflets and four non macroscopically calcified leaflets were further analysed by electron microscopy. Calcified particles, fibres and compact minerals (Fig. 3A and B, S6) were found on both the aortic and ventricular surfaces. The calcified particles were predominantly detected on the surfaces (irrespectively of anatomical location (aortic or ventricular side)) of all leaflets (Fig. 3C), suggesting a possible mechanism leading to surface deposition. In contrast, the remaining minerals appeared to surface due to structural growth originating from inside the leaflet, as confirmed by microCT data, which showed that calcifications were primarily found in the middle of the leaflet walls rather than the surface. While previously, differences between the calcification extent of the fibrosa and ventricularis have been reported in bioprosthetic valves, especially porcine aortic valves, no evident differences were found in the bovine pericardial valves investigated in this study [48]. This is explained by the different tissue architecture between the porcine aortic tissue and the bovine pericardium, and, possibly by the higher sensitivity of the analytical methods used herein, leading to detection of calcification on both sides in all leaflets. To ensure that none of these structures result from precipitation

due to pretreatment or storage procedures, four expired non-implanted leaflets were processed in the same way and presented no minerals (Fig. 4B). Thus, it was concluded that the main calcification processes in implanted bioprosthetic valves lead to deposition of calcified particles and their surface and extensive mineralisation of the collagen network. As collagen mineralisation was identified inside the leaflet wall and has not been identified in native valvular leaflets (at very least to no comparable extent), it hints toward a mineralisation process specific to bioprosthetic valvular tissue that initiates within the chemically fixed pericardial tissue.
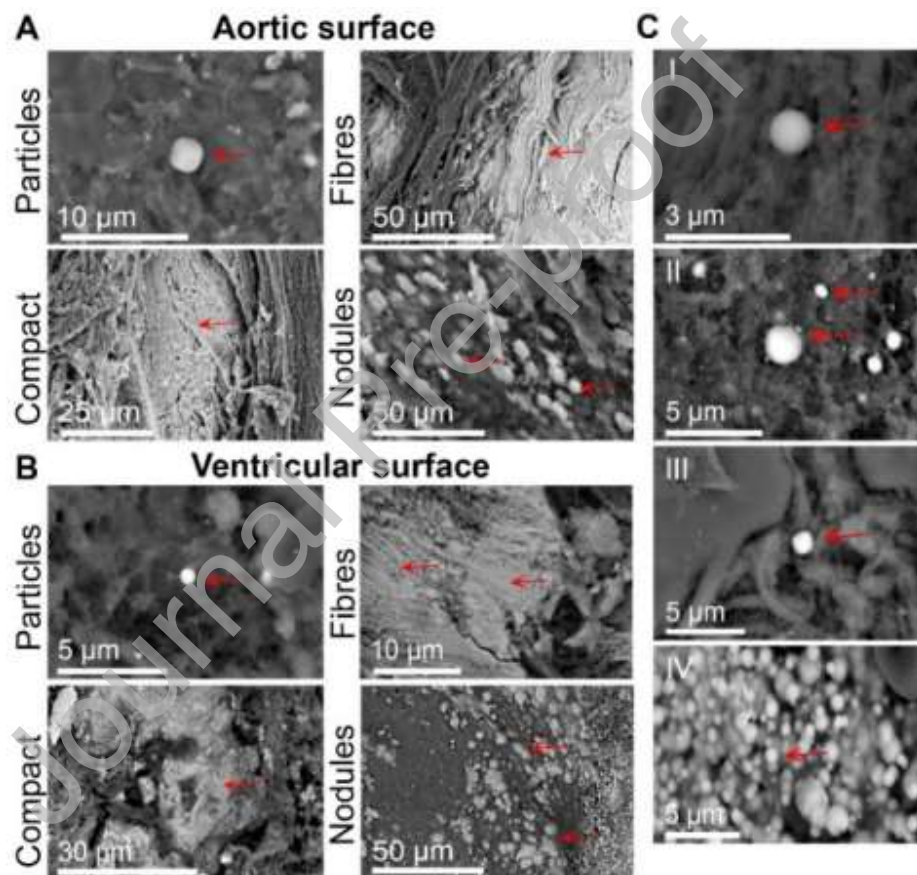

Fig. 3. Mineral presence on the aortic and ventricular side surfaces of bioprosthetic cusps. *Morphologically different minerals were found; calcified particles, calcified fibres, compact calcification and nodules on the **(A)** aortic and **(B)** ventricular surfaces. **(C)** Calcified particles were observed regardless of the degree of calcification or anatomical location. Scanning electron micrographs of particles found on **I** non-macroscopically calcified, and **II**, **III** and, **IV** macroscopically calcified explanted leaflets of increasing calcification percentages.*

The fibres likely stem from mineral precipitation on the collagen [49]. In contrast, the vast presence of the calcified particles both within and on the leaflet wall surface suggests a process of cellular origin (e.g. from macrophages or other cells, cell-derived structures or particles originating from the blood), as previously suggested [50-53] for the same particles (same shape, size and composition) in native valves. Furthermore, similar particles have also been observed in tumour vasculature [54], the Bruch's membrane of the eye [55, 56], and other cardiovascular tissues[57] suggesting a host-environment origin shared between several pathologies.

Early-stage mineralisation contains mineralised particles and fibres

To assess the presence of early stages of mineral formation, we investigated non-calcified failed explanted bioprosthetic valve leaflets with high resolution optical and electron microscopy (Fig. 4). Calcified particles were identified (Fig. 4, S7 and S8) through Von Kossa staining and confirmed by nanoanalytical techniques in three out of four non-macroscopically calcified leaflets. Anatomically, they were scarcely observed at various positions on the valve surfaces. EDX analysis indicated that these were always composed of calcium, phosphate and magnesium (Fig. S7).

Backscattered electron microscopy also revealed the scarce presence of calcified fibres and fibrils made of calcium and phosphate (Fig. 4, S7) in half of the investigated non-macroscopically calcified leaflets. Correlative confocal and second harmonic generation (SHG) imaging (Fig. 4A and S8) indicated that these calcified fibres colocalised with collagen fibres, indicating a process of collagen mineralisation, well in line with the SEM investigations (Fig. 2). In contrast, SHG imaging suggests that the calcified particles were entrapped within collagen network gaps rather than deposited onto fibres and were not locally associated with collagen mineralisation (at least at the initial stages). This spatially independent occurrence of the two minerals (calcified collagen fibrils and calcified particles) further supports the existence of two distinct mineralisation phenomena, which may contribute to the creation of larger mineral accumulations (Fig. 2 and 3) over time.
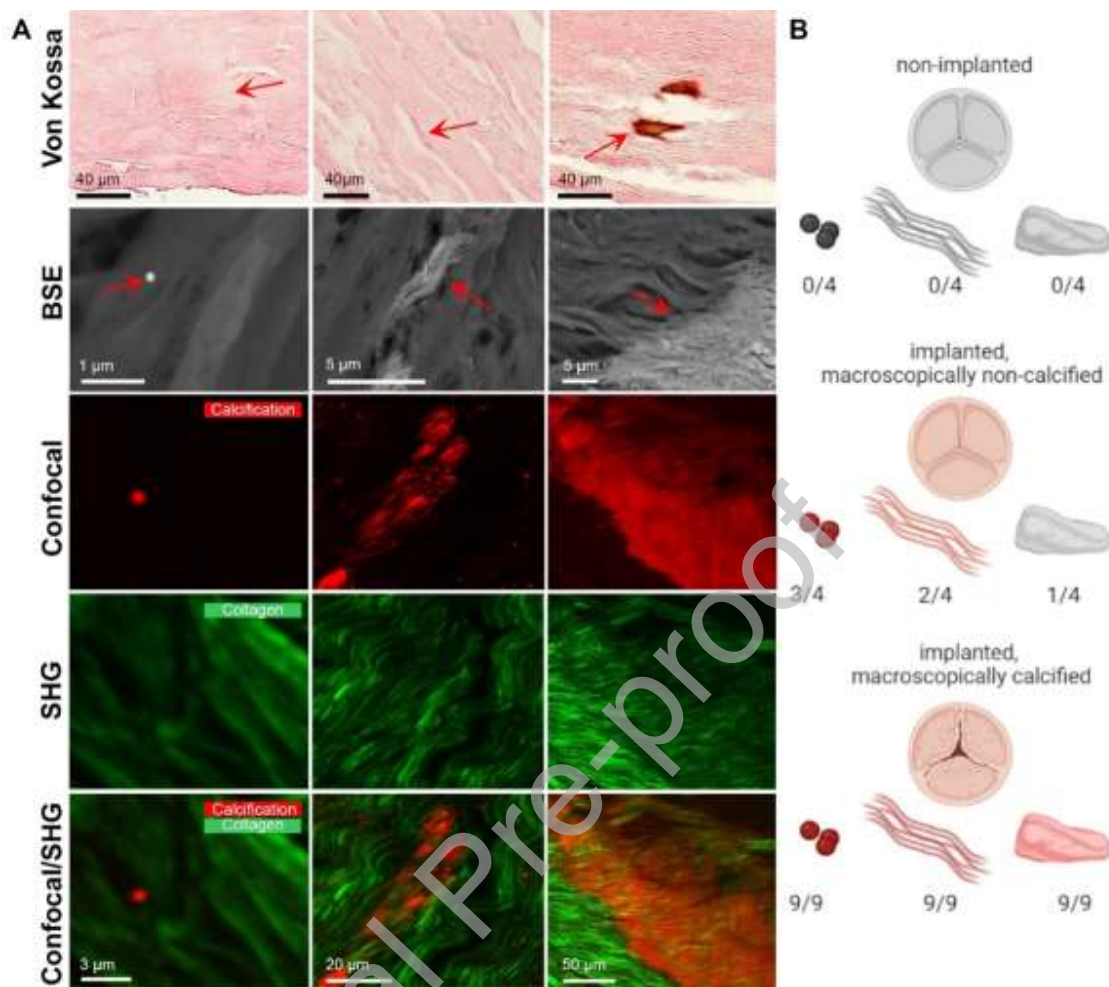
Fig. 4. High-resolution imaging analysis of minerals within non-calcified bioprosthetic cusp tissue. (A) Calcified regions were observed in Von Kossa stained samples as brown/black spots indicated by arrows. High resolution imaging by scanning electron microscopy enabling morphological and chemical charactierzation of the mineral (BSE, arrows and EDX, see SI Figure S7). Confocal microscopy of the mineral (red), overlaid with SHG data showing the collagen network (green) enables co-localization analysis of the mineral with collagen. Calcified particles, fibres and compact calcifications were identified. (B) Prevalence of mineral structures (particles, fibres, compact (macro and micro) calcification) found in non-implanted (n=4), implanted non-macroscopically calcified (n=4) and implanted macroscopically calcified (n=9) leaflets, analysed by micro and nanoscale characterisation techniques.

Microscale characterisation of tissue alterations reveals changes to the collagen structure

Due to the seemingly abundant bioprosthetic tissue-specific collagen mineralisation process, we investigated potential non-calcific tissue alterations that could contribute to its initiation or/and progression. Data acquired from H&E stained sections obtained from the analysed leaflets indicated a loss of cellular components and the thickening of the fibrous network, resulting in more compacted tissue in implanted

valves (Fig. S9) compared to non-implanted ones. PicroSirius Red staining further evidence that the collagen network was vastly altered in implanted valves (Fig. S9), even in the absence of calcific deterioration. To gain global information on the collagen network organisation, selected representative leaflets were investigated by scanning small angle x-ray scattering (SAXS). A new non-implanted bioprosthetic valve leaflet, an explanted macroscopically non-calcified and an explanted macroscopically calcified leaflet were analysed (Fig. 5) [29]. A leaflet presenting low degrees of calcification was selected to assess the differences in collagen organisation between calcified and non-calcified regions on the same leaflet. Verifying the histological findings, SAXS analysis indicated differences in the organisation and orientation before and after implantation, even in the absence of macroscopic calcification.

On the one hand, the non-implanted bioprosthetic valve leaflet presented homogeneously a typical fibrillary diameter of 141.46 ± 1.44 nm (Fig. S10) and a scattering pattern characteristic of healthy collagen (Fig. 5 and S11) ('eye brow' pattern), known to originate from the triple helix structure of the tropocollagen molecule [58]. Similarly, the q-regime corresponding to the d-spacing of the fibril in bundle – corresponding to the collagen fibril and the tropocollagen 5th order collagen peak orientation (Fig. 5A) were homogeneous throughout the leaflet, as expected (Fig. 5B, angle dependency of the orientation encoded in the colour wheel). On the other hand, while the non-calcified explanted leaflet retains to some extent its homogeneous orientation, some areas present low-intensity collagen fibril diameter reflections and a lower degree of orientation for the 5th collagen peak. These changes are visible in the orientation of the bundle structure of the fibirls, the 5th collagen peak (Fig. 5B, parts of the commissures and free edge appear as black), and the scattering pattern (Fig. S12). However, no changes were seen on the collagen nanostructure, as observed from the object orientation in the $0.417 < q < 0.450$ nm^{-1} collange/mineral q-equivalent domains (CNQED) (Fig. 5B), suggesting the fibrillary structure with the nanodomain of the tropocollagen molecules remaining unaffected.

Similarly, heterogeneity was observed in the calcified leaflet even in non-mineralised areas (Fig. 5B), with comparable orientations observed for the collagen diameter and the CNQED (shown in the same colour range in Fig. 5B) for mineralised and non-mineralised areas. This suggests that the structures within

the calcified regions follow the natural collagen fibril orientation (Fig. 5B and S13) and supports an intra-

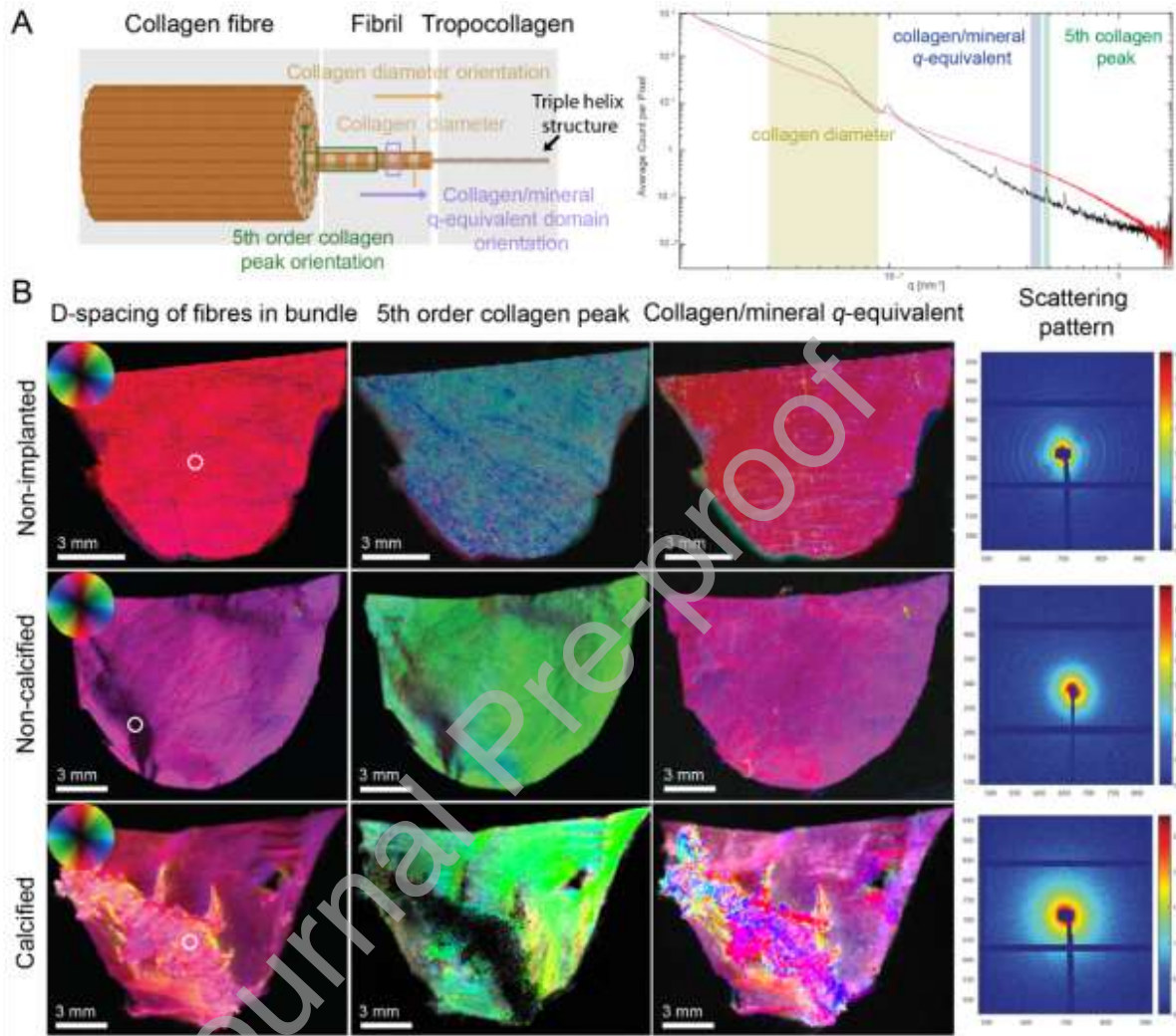or inter-fibrillar mineralisation of the collagen structure.

Fig. 5. Collagen network SAXS analysis in bioprosthetic valvular leaflets. *(A) Schematic of collagen structure and diffraction peak plot indicating the collagen diameter, 5th collagen peak and collagen/mineral q-equivalent domain. Black and red curves representing the non-mineralised and mineralised samples respectively (B) Orientation analysis of (I) the d-spacing peak of fibres in bundles (aka collagen diameter) (II) 5th order collagen peak, (III) $0.417 < q < 0.450$ nm^{-1} collagen/mineral q-equivalent domain and (IV) representative scattering patterns of regions marked by a circle, in a non-implanted, a non-calcified explanted and a calcified explanted leaflet. Within this HSV (Hue, Saturation and Value) representation, hue gives information on the orientation according to the colour wheel, saturation on the degree of orientation and the value on the density of the scattering material.*

Additionally, an altered main orientation of the fibrillar structure within the non to low-calcified

regions is associated with a mineralisation fingerprint (visible as a yellow halo around the mineralised part)

(Fig. 5B). In these regions, a change in the collagen fibrillar diameter from the healthy diameter calculated to be 144.29 ± 3.09 nm towards 111.16 ± 6.06 nm in the region within the mineralisation front is observed (Fig. S10). Moreover, the characteristic scattering pattern (Fig. S13 and S14) is found to gradually disappear closer to the mineral, suggesting either damages in the tropocollagen helical structure or the formation of an additional overlapping phase suppressing it. Finally, collagen structure changes can be seen from the change in orientation of the 5th collagen peak in regions where the CT does not show any mineralisation (yellow regions on 5th collagen peak orientation) (Fig. 5B). These results illustrate the extent of non-calcific collagen alterations, highlight the impact of implantation on bioprosthetic valvular tissue, and reveal at least a partial connection between such non-calcific alterations and calcific degeneration.

Macroscopic distribution of haemodynamic and biomechanical indicators correlate with calcific damage

To study alterations in the arterial wall such as atheroma plaque through the growth of endothelial lesions or calcification, WSS manifolds have been established as important topological features to explore. In fact, singular points and so-called limiting streamlines parallel to the the WSS vector were first reported in the trileaflet native aortic valve in the study by Ge and Sotiropoulos [59]. They hypothesised that WSS topological features have a link with calcification. However, no rigorous pathway was proposed. Later, in a series of work by Arzani and Shadden [60], the concept of WSS topology through WSS Lagrangian Coherent Structures (LCS), WSS exposure time, and WSS fixed points were introduced in detail to correlate blood flow with cardiovascular diseases. A strong link between WSS topology and near-wall mass transport and residence-time was provided, which explains one possible link to calcification (e.g. near-leaflet biochemical/particle accumulation leading to the initiation of cascade of reactions in calcification). Thereafter, the topological shear variation index (TSVI) metric considered in this study was proposed by Morbiducci *et al.* [61] as a surrogate for the aforementioned topological features. As summarised in [60], WSS topology either affects vascular disease by influencing endothelial cells (dramatic variation in WSS direction and magnitude) or by promoting near-wall atherogenic biochemical accumulation (e.g.,

monocytes/macrophages). We hypothesised that similar topological descriptors may also be employed to predict zones prone to the aforementioned tissue alterations in bioprosthetic aortic valves.

We, therefore, explored correlations between macroscopic calcific alterations and specific temporally and spatially varying wall-shear-stress fields using high-fidelity simulations of the coupled blood flow and leaflet mechanics. We investigated the local distribution of haemodynamic and biomechanical metrics such as time-averaged wall shear stress (TAWSS), oscillatory shear index (OSI), topological shear variation index (TSVI), scalar strain (SS) and von Mises stress (vMS) using two valvular geometries (ULth0 and Vlth30, Fig. S15). Two different valve geometries were considered in the computational part of this study (Fig. S15). The Vlth30 geometry was indeed chosen as the *in vitro* experimental data used to rigorously validate the FSI simulations were in very good agreement with numerical results obtained with this geometry. The experimental validation using *in vitro* tomographic particle imaging velocimetry data [70] of the simulation-based flow field quantities (time-averaged and fluctuating velocities) downstream of the valve as well as leaflet kinematics (area at the vena contracta and leaflet motion during the opening phase) can be found in Corso *et al.* [37, 62]. Additionally, the ULth0 geometry was chosen to investigate the impact of strong periodic oscillations in leaflet motion (see Fig. S19) on the distribution of haemodynamic and biomechanical indicators studied and to analyse the link between these motions observed at peak sytole and calcification.

For the ULth0 geometry, we observed high TAWSS in the central parts of the leaflet belly on the ventricular side (Fig. S16A), in line with the tendency of mineral accumulation noted from microCT measurements while on the aortic side, the highest TAWSS values were found at the free edge of each leaflet and close to the leaflets' attachment to the crown (Fig. 6A). The concentration on the aortic side of high TAWSS valve at the attachment line was even more noticeable in the case of the Vlth30 leaflet geometry.

Furthermore, the area with higher TAWSS values at the commissures, fixed edges and annulus on the aortic side (Fig. 6A and S16A) correspond to areas rarely found calcified in the analysed explanted bioprosthetic heart valve specimens. The elevated TAWSS values at the attachment curve and annulus on the aortic side

could result from restricted motion and the narrowness of the flow regions between the leaflets and the crown (Fig. S15) to which the leaflets are attached, promoting more intense shear forces due to blood flow. The WSS values (without time-averaging operation) between the aortic and ventricular sides were compared from the time evolution of the spatially averaged WSS values presented in Fig. 6C and Fig. S16B. We noted that, on average for the Vlth30 geometry, the WSS values (maximum or mean) on the ventricular side are 3.9 times higher than those on the aortic side while for the ULth0 leaflet geometry, the maximum or mean WSS levels on the ventricular side are 2.5 times higher. More specifically, in the Vlth30 case, the maximum spatially-averaged WSS values were equal to 3.6 Pa and 0.8 Pa on the ventricular and aortic sides, respectively. As for the ULth30 case, the maximum mean WSS magnitude reached a similar value of 3.6 Pa on the ventricular side but a twice as large value as the one for the Vlth30 case (1.4 Pa) on the aortic side. The results from the FSI simulations presented in Salman *et al.* [69] showed that the ratio of the WSS values between ventricular and aortic surfaces averaged over time and space ranges from 6.2 to 8.1 depending on whether non-calcified or calcified leaflets are envisaged by changing Young's modulus in the simulations. These values were twice to thrice as large as the ratios calculated from the FSI simulations in the present study. Besides, in Salman *et al.* [69], the maximum value over time of the spatially averaged WSS magnitude was equal to 14.4 Pa on the ventricularis surface and 1.9 Pa on the fibrosa surface. Although the value on the aortic side was comparable to that calculated in the current computational study on the aortic side of the ULth0 leaflets, the value obtained in [69] on the ventricular side was four times as high as the one calculated in the ULth0 case. The discrepancies pertaining to the levels of WSS may be a consequence of the use in Salman *et al.* of unrealistic isotropic elastic material properties to model the native aortic valve leaflets' response both in healthy and calcified conditions.

In another study published by Cao and Sucosky [71], values of TAWSS were calculated for i.a. a model of porcine tricuspid valve for which the material properties of the leaflets were given by the isotropic three-parameter hyperelastic Mooney-Rivlin constitutive law. In [71], the ratio of the spatially and temporally averaged WSS magnitude between the ventricularis and fibrosa sides was equal to 5.2 (against 3.9 and 2.5 in the present study) and the maximum total WSS magnitude at peak systole was about 12 Pa on the

ventricular side and about 3 Pa on the aortic side and these values were mainly located at the free edge of the leaflets on both sides. As shown in Fig. 6A, the maximum values of TAWSS in the current study were found on the aortic side at the free edge (ULth0 geometry) and at the attachment curve (Vlth30 geometry) reaching an instantaneous value of WSS magnitude up to 20 Pa (ULth0 geometry) and 10 Pa (Vlth30 geometry) as presented in Fig. 6C. On the ventricular side, the highest TAWSS values were found on a horseshoe-like region (Fig. S16A) with values of instantaneous WSS magnitude of 20 to 24 Pa for both leaflet geometries (cf. Fig. S16B). Worthy of note to justify the discrepancies between the WSS values as well as the ratio of these values between ventricular and aortic sides in Cao and Sucosky [71] and the ones presented in this work is the difference in the constitutive laws for the leaflets employed in [71], i.e. a model characterising untreated porcine leaflet response, as compared to that employed in current study, which took into account the effects of anisotropically distributed collagen fibres in bovine pericardium embedded in an isotropic extracellular matrix after a glutaraldehyde fixation treatment (35).

In line with the regions highlighted by high TAWSS values, the von Mises stress (vMS) in the leaflets was maximum at commissures, at the attachment line as well as in the middle of the free edge, regions where the scalar strain (SS) is minimum. In contrast, on the ventricular side, the distribution of SS values were congruent with the distribution of TAWSS values. These observations are in line with the cumulative increased tendency of mineral accumulation in the centre of the belly in the analysed leaflets (Fig. 1C).

In relation to the OSI and TSVI indicators, large values were mainly identified in the centre and top parts of the leaflet belly predominantly on the aortic side (Fig. 6A and S16). Higher OSI and TSVI could contribute to the triggering of collagen network alterations, leading to subsequent collagen mineralisation; supporting the hypothesis that time-varying haemodynamic wall shear stresses leading to the repetitive expansion and contraction of the leaflet surface may contribute to valvular failure. In this respect, the TSVI distribution presented similar patterns (with different magnitudes) on both the aortic and ventricular sides, with higher values observed at the top half of the leaflet (Fig. 6B and S16), which is aligned with the mineral content (calcified particles and nodules) observed on the aortic and ventricular leaflet external surfaces as identified through the SEM analysis.

Regarding the comparison of the OSI indicator between the values presented in [71] and the values in the current computational study, on the ventricular side, an OSI value averaged over the three leaflets of 0.06 was evaluated in [71] against a value of 0.033 and 0.013 for the ULth0 and Vlth30 geometries analysed in this study. Conversely, on the aortic (fibrosa) side, a spatially averaged OSI value of 0.26 found in [71] was compared to the 0.2 and 0.13 values achieved from the investigated ULth0 and Vlth30 cases. The origin of the 1.3 to 2 times higher averaged OSI values revealed in [71] as compared to those obtained in this work could be connected to the inflow boundary conditions imposed in [71], which led to a twice smaller flow acceleration and four times larger flow deceleration as compared to the inflow conditions imposed in the numerical part of this study.

The association of blood flow patterns with the presence of minerals on the leaflet surface was also evaluated through computations of the RRT (i.e. the time blood elements spend at a specific location on the surface derived from the OSI and TAWSS indicators) and blood vorticity (Fig. 6B). Similarly to the distribution of OSI, on the aortic side, higher RRT values were found in the centre of the leaflets, i.e. in the belly region. However, in contrast to the TSVI and OSI distributions and in a comparable way to the TAWSS distribution on the aortic side, large RRT values were also present close to the annulus and attachment curve of the leaflets to the crown.

The smaller vorticity values in the belly region of the leaflets can be explained by the low flow velocities simulated in the central regions of the belly, which are associated with higher residence time and OSI (Fig. 6B and S16). The fluid-structure interaction simulations also indicated higher flow vorticity magnitudes near the free edge of the leaflets, which could explain the absence of minerals in this region until later degeneration stages (once the leaflet becomes highly calcified, as observed through microCT imaging). This could be due to the increased flow momentum (related to flow turbulence) preventing higher mineral deposition, triggered by the generation of vortical structures subsequent to the shear-promoting flutter leaflet motion.
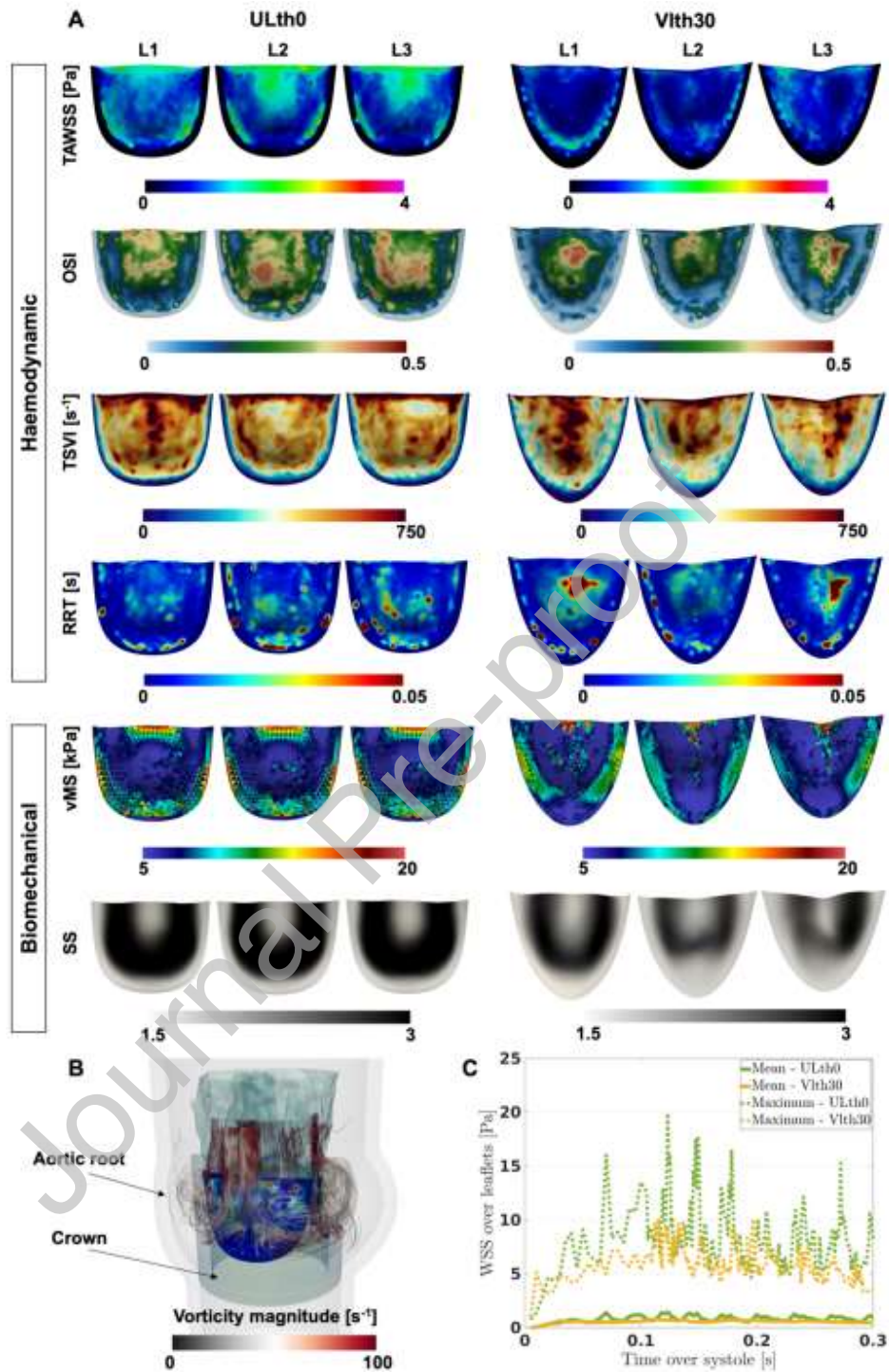
Fig. 6. Spatial distribution on the aortic surface (fibrosa) of the three leaflets using a fibre-reinforced material model and the leaflet geometries referred to as ULth0 and Vlth30. *(A) Distributions of the time-averaged wall shear stress (TAWSS), oscillatory shear index (OSI), relative residence time (RRT), topological shear variation index (TSVI), von Mises stress (vMS), scalar strain (SS) (B) Streamlines coloured with the vorticity magnitude in the vicinity of the leaflets. The leaflet is colour-coded with the relative residence time and an iso-surface of turbulent kinetic energy (equal to 0.08 m²/s²) issuing from the leaflets' free edges is displayed. Distributions in the aortic side of the RRT are shown, and the vorticity*

magnitude of blood in the aortic root. (C) Time evolution of maximum and spatially averaged wall shear stress onto the aortic side of the three leaflets of both valve designs (Vlth30 and ULth0).

Considering the two leaflet geometries designed for the computational study during the peak systolic phase, the Vlth30 case (Fig. S15) presented a distinct bi-directional flutter motion as opposed to that of the ULth0 leaflet geometry, which was characterised by an axisymmetric periodic flutter motion (Fig. S15 and Fig. S19). Moreover, both employed leaflet geometries (Fig. S15 and S16) shedded light on a possible link between flutter instability [36, 37] of the leaflet motion at peak systole and calcification. This possible link is supported by the fact that the high OSI and TSVI regions in both geometries and particularly on the aortic seemed to be located where a curvature change in the leaflet motion leading to a stretching of the leaflet was noted as indicated by high values of scalar strain (Fig. 6A and S16) and a similar region was found to be calcified in all macroscopically calcified leaflets examined with microCT (Fig. 1B and 1C). Interestingly enough, this curvature change in the leaflets and ensuing high scalar strain values were a consequence of the fluttering leaflet dynamics over peak systole.

In order to more accurately correlate the location of the macroscopic calcific structures identified through the microCT analysis and the location revealed by judiciously chosen haemodynamic and biomechanical indicators from the coupled blood-leaflet dynamics simulations, the contributions of three indicators, chosen either on the aortic side or on the ventricular side based on their qualitative agreement with the microCT spatial distribution of calcification (see Fig. 6A and Fig. 1C), were combined in order to obtain a reconstructed calcification intensity (out of the formulation and resolution of a previously described optimisation problem). The reconstructed calcification field was then directly compared to the observed calcification intensity (calculated from the cumulative spatial distribution of calcification from microCT images) in the macroscopically calcified leaflets considered (Fig. 7). The regression analysis indicated a good agreement between the two calcification patterns (as brought out by the relatively high value of 0.74 for the coefficient of determination R^2 for the regression based upon the testing data set) which corroborated the validity of the selected hemodynamical and biomechanical indicators and demonstrated the adequacy of the resulting reconstructed calcification equation (i.e. Eq. 8) for the assessment of the degeneration and

calcification of bioprosthetic aortic valves. It is worth noting that the relative contribution (i.e. divided by the reconstructed calcification intensity averaged over the three leaflets) of each term in Eq. 8 (averaged over the three leaflets of both valve geometries) amounted to 44.5% for the TSVI term on the aortic side, 65.5% for the TAWSS term on the ventricular side, the contribution of the shear strain term on the aortic side being negligible. Furthermore, it is interesting to mention that the calcified area estimated from the microCT measurements on all calcified leaflets represented 31.5% of the total leaflet surface. As shown in Table 1, for the ULth0 leaflet geometry, the prediction from the reconstructed calcification intensity led to a calcific region area divided by the total leaflets' area ranging from 30% to 33% depending on the considered leaflet. This remarkable agreement with the microCT estimation further supported the interest of the introduced novel approach (Eq. 8) for the prediction of zones with calcific alterations resting on the calculation of the TSVI indicator on the aortic side of the leaflets and TAWSS on the ventricular side and to a lesser degree, on the leaflets' scalar strain. With regard to the Vlth30 valve geometry, the area occupied by the region with values for the reconstructed calcification intensity larger than 0.9 (i.e. red zones in Fig. 7C) varied from 16% to 28% (cf. Table 1). These values of calcified area were smaller than that originating from the cumulative spatial distribution built on microCT data of all calcified leaflets but they were nearly commensurate with the values presented in Table S1 (for valve numbers 3 and 7) of the supplementary information.

Finally, the sensitivity of the prediction accuracy to variations in the coefficients of the model given by Eq. 8 was analysed and the corresponding graphs in Fig. S18 were provided. The bar graphs showed that the accuracy evaluated with the coefficient of determination (R^2) was strongly (almost quadratically) influenced by variations in the coefficients C_3 multiplying the TAWSS term and changed linearly with a slope of about 0.5 with the coefficients C_1 multiplying the TSVI term. Changes in the exponents given by coefficients C_2, C_4 and C_6 very slightly reduced the accuracy of the model and in the wake of the foregoing negligible contribution of the SS term, modifications in the C_5 coefficient had almost no effect on the accuracy of the model.
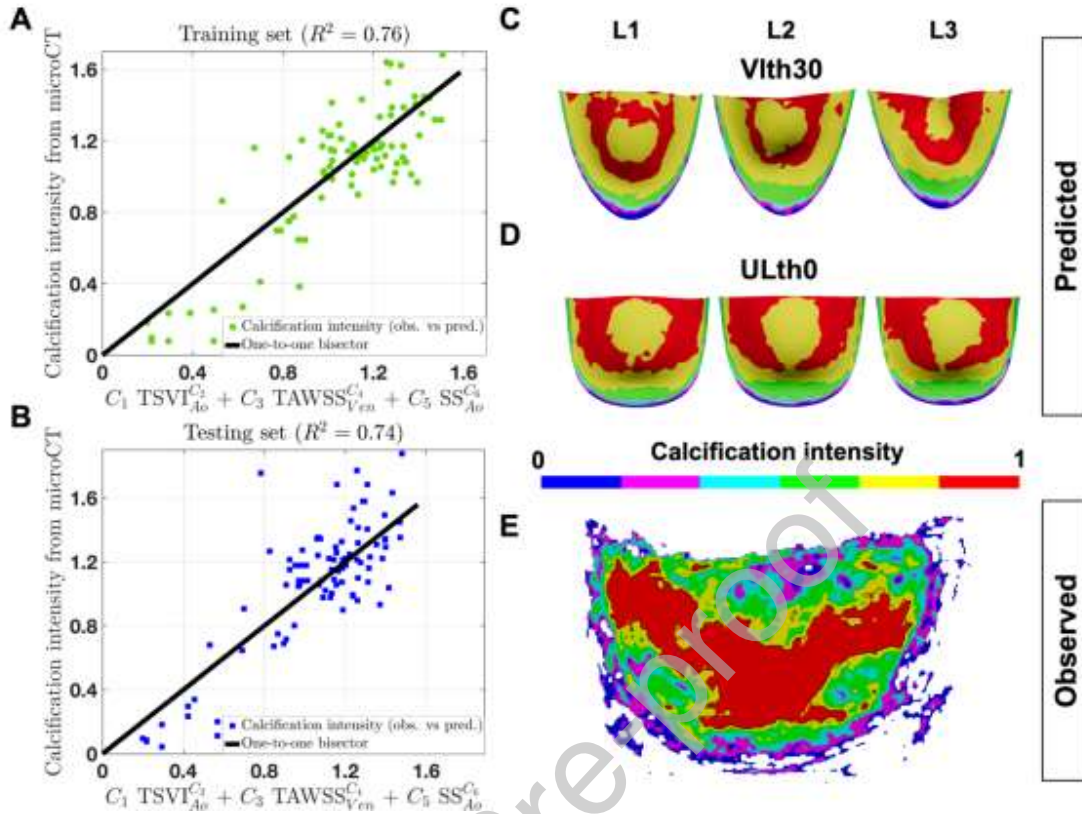
Fig. 7. Comparison between predicted calcification intensity and the observed calcification intensity. *Regression analysis showing a good correlation between the predicted and the observed calcification analysis using a training data set (**A**, $R^2 = 0.76$) and a testing data set (**B**, $R^2 = 0.74$). Predicted calcification intensity in Vlth30 (**C**) and ULth0 (**D**) valve geometries computed using the contribution of the TSVI, TAWSS and SS indicators. (**E**) Observed calcification intensity as observed through the microCT analysis for comparison.*

Table 1: Area of the calcific regions for both valve leaflet geometries predicted from the reconstructed calcification intensity field derived from the FSI simulations.

Valve design reference	Physical time simulated	Leaflet	Calcified area stemming from the reconstructed calcification intensity from FSI simulations (Eq. 8)
Vlth30	0.3s	L1	**22%**
		L2	**16.5%**
		L3	**28.5%**
ULth0	0.3s	L1	**33.5%**
		L2	**30.5%**
		L3	**30.5%**

Conclusions

Our multiscale multimodal analysis of bioprosthetic heart valve explants enabled a in-depth, systematic characterisation of minerals with full histoanatomical context and the documentation of the extensive presence of calcified collagen fibres and fibrils within all macroscopically calcified explanted bovine valve leaflets analysed. Even though older transmission electron microscopy studies show collagen mineralisation in failed porcine bioprosthetic valves, and the involvement of collagen in mineralisation has also been discussed in *in vitro* studies on fixed pericardium [63-66], the extent and severity of such calcification in current widely used bovine bioprosthetic valves have not been apparent. Notably, such collagen mineralisation has not been reported in native aortic valves (Fig. S4) or other native soft tissue, or at least not to a comparable extent. This finding suggests an underlying mechanism particularly prevalent in bioprosthetic valves, likely due to controversial tissue pretreatments and fixation, which may be preventable using emerging tissue treatment methods optimized based on nanoanalytical investigations enabling detection of early stage mineralizations. Notably, identifying early-stage mineralisation, such as the ones identified in this work by nanoanalytics, may offer an accelerated route for prescreening alternative tissue treatment options.

Finally, we highlight the importance of considering non-calcific tissue alterations to understand bioprosthetic valve structural failure and their role in mineralisation induction. The discovered disruptions to the collagen network and their link to biomechanical stress have been suggested to be one of the primary reasons limiting durability and playing a role in calcification induction (acting as nucleation sides) [21, 49, 64, 67, 68].

With regard to the computational part of the study, to the best of our knowledge, it is the first time that the topological shear variation index (TSVI), originally proposed by Morbiducci *et al.* [61] to highlight the link between flow disturbances and vascular lesions after carotid bifurcation endarterectomy, is evaluated at the surface of bovine pericardial aortic valves from high fidelity fluid-structure interaction simulations. In addition, by analysing and quantifying the distribution of calcification from microCT measurements and through the resolution of a least-square minimisation problem resulting in high values for the coefficient of determination (R^2), a new prediction tool in the form of an equation to calculate a

calcification intensity is proposed. The equation is dependent upon the TSVI, TAWSS indicators and to a lesser degree upon the SS indicator at the leaflet surfaces. Interestingly, we note that the valve with the Vlth30 leaflet geometry, for which a limited and asymmetric flutter motion at peak systole is noted, presents a reduced predicted calcified area as compared to the one predicted from the FSI simulations with the ULth0 leaflet geometry, whose flutter motion during systole is characterised by periodic and large displacement magnitude. These observations thus suggest the existence of calcification-prone valve designs, the latter also playing a role in the unstable leaflet motion at systole. It is also worthwhile to emphasise the 1.5 to 3 times smaller values of the ratio between ventricular and aortic TAWSS noted in this work for glutaraldehyde-pretreated pericardial aortic valves as compared to the values presented in other computational studies of the literature that focus on modelling the dynamics of native tricuspid aortic valves together with blood mechanics.

Main limitations of the current study include the limited number of explanted valves samples available, as well as the lack of information on the valve orientation (coronary vs. non-coronary leaflets). However, the high abundancy of the collagen fiber mineralization (100% of the macroscopically calcified leaflets contained extensive amounts of mineralized fibres) indicates high prevalence of the observed mineral structures, even based on this study population limited in size. Also, the sex of the animal tissue donors remained undisclosed, even though differences in mineral composition and morphology between male and female animals and humans have been described [47]. Another limitation of our study is the assumption that the degeneration mechanisms are progressive processes, as analysing the same valve at different time points to gain quantitative data on non-calcific and calcific processes is not technically feasible. Thus, we can only indirectly hint at the anatomical origins of mineral nucleation and collagen network alterations in explanted valves based on the obtained data. However, the correlations between mineral extent and distribution and implantation duration supports the assumption of a progressive process.

Additionally, a limitation in the fluid-structure interaction (FSI) computational study concerns the reduced time span (0.3 seconds) considered over systole, as compared to the time span of the valvular degeneration mechanisms, which can last for 10 to 15 years. Alterations in the collagen structure could

indeed be induced throughout the whole cardiac cycle (i.e. during both the systolic and diastolic phases) and over the valve bioprosthesis lifetime. Moreover, to take into account alterations due to the progressive degeneration in the glutaraldehyde-fixed bovine pericardium tissue, as a prospective extension of the present computational work, it is planned to study changes in the haemodynamic and biomechanical indicators in the aftermath of modifications in the anisotropic part of the constitutive law (cf. Eq. 1) used to model leaflets' material response. These modifications will represent the progressive collagen fibres' calcific alterations. Despite this, trends in the proposed haemodynamic (i.e. based on wall shear stress vector) and biomechanical indicators (i.e. based upon valve leaflets' motion) have been identified, and the spatial distribution of a defined calcification intensity observed from microCT measurements has been fitted and convincingly correlated to the distribution of a predicted calcification intensity depending on thoughtfully chosen haemodynamic and biomechanical indicators. It is important to mention that the prediction accuracy, derived from the least-square minimisation problem, relied on the reference calcification intensity computed from microCT data obtained from the 14 leaflet samples. Therefore, in a prospective study, it would be worthwhile to calculate the prediction accuracy of the proposed model (Eq. 8) using spatial distributions of calcification obtained from calcified leaflet specimens that differ from those utilised in fitting the coefficients through the minimisation procedure. Furthermore, the absence of coronaries in the aortic root model used for the three-dimensional FSI simulations could represent a limitation as coronary flows have an influence on the flow in the sinus of Valsalva. Notwithstanding this, within the scope of the computational part of this study, i.e. to provide a connection between unstable leaflet motion, haemodyamic and biomechanical indicators and calcification-prone zones, the effects of such coronary flows are less prominent than those due to the leaflet motion during systole.

Further *in vitro* experimental work building on our observations may be performed to assess the effect of biomechanical forces in the induction of calcific and non-calcific collagen alterations and aid the understanding of the exact processes leading to collagen mineralisation (and which non-calcific alterations enable initial mineral nucleation).

In addition to the above new insights, our work offers a route to seamlessly integrate nanoanalytical characterisation in the clinicopathological analysis to investigate histoanatomical localisation and characteristics of minerals in a wide variety of tissue samples. This route paves the way for larger clinical studies with significantly larger sample numbers, evaluating diagnostic (and/or prognostic) value of mineral characteristics in soft tissues.

Author contributions: E.T., S.B., T.C., D.O. and I.K.H conceived the study. E.T. performed experimental microscopy studies, analysed and interpreted data and created the first draft of the manuscript. P.C. performed the FSI computational simulations, analysed and interpreted the computational data, produced the results and figures for the computational part of the study, performed the comparative analysis (microCT vs simulation data), devised and wrote the computational part of the study, R.Z. performed micro CT scans

and 3D analyses, J.A., C.A. and M.L performed SAXS synchrotron measurements, analysed the SAXS data

and wrote the SAXS method part, P.P.H. collected samples and patient data. All authors discussed the data

and edited the manuscript. D.O. provided input for the computational part, T.C. supervised the clinical part

and I.K.H. supervised the multiscale characterisation work and the overall study.

Conflicts of Interest: The authors declare that there is no conflict of interest.

Data and materials availability: All data and materials needed to evaluate the conclusions of this paper

are present in the main text or supplementary materials. Processable data files can be obtained from the

authors.

References

[1] V.T. Nkomo, J.M. Gardin, T.N. Skelton, J.S. Gottdiener, C.G. Scott, M. Enriquez-Sarano, Burden of valvular heart diseases: a population-based study, Lancet 368(9540) (2006) 1005-11.

[2] R.F. Weska, C.G. Aimoli, G.M. Nogueira, A.A. Leirner, M.J. Maizato, O.Z. Higa, B. Polakievicz, R.N. Pitombo, M.M. Beppu, Natural and prosthetic heart valve calcification: morphology and chemical composition characterization, Artif Organs 34(4) (2010) 311-8.

[3] A. Bonetti, M. Marchini, F. Ortolani, Ectopic mineralization in heart valves: new insights from in vivo and in vitro procalcific models and promising perspectives on noncalcifiable bioengineered valves, Journal of thoracic disease 11(5) (2019) 2126-2143.

[4] F. Oveissi, S. Naficy, A. Lee, D.S. Winlaw, F. Dehghani, Materials and manufacturing perspectives in engineering heart valves: a review, Materials Today Bio 5 (2020) 100038.

[5] S. Chitsaz, N. Gundiah, C. Blackshear, N. Tegegn, K.S. Yan, A.N. Azadani, M. Hope, E.E. Tseng, Correlation of calcification on excised aortic valves by micro-computed tomography with severity of aortic stenosis, The Journal of heart valve disease 21(3) (2012) 320-7.

[6] P. Mazur, E. Wypasek, B. Gaweda, D. Sobczyk, P. Kapusta, J. Natorska, K.P. Malinowski, J. Tarasiuk, M. Bochenek, S. Wronski, K. Chmielewska, B. Kapelak, A. Undas, Stenotic Bicuspid and Tricuspid Aortic Valves- Micro-Computed Tomography and Biological Indices of Calcification, Circ J 81(7) (2017) 1043-1050.

[7] D.A. Lerman, S. Prasad, N. Alotti, Calcific Aortic Valve Disease: Molecular Mechanisms and Therapeutic Approaches, Eur Cardiol 10(2) (2015) 108-112.

[8] M.A. Gomel, R. Lee, K.J. Grande-Allen, Comparing the Role of Mechanical Forces in Vascular and Valvular Calcification Progression, Front Cardiovasc Med 5 (2018) 197.

[9] M.R. Labrosse, C.J. Beller, M. Boodhwani, C. Hudson, B. Sohmer, Subject-specific finite-element modeling of normal aortic valve biomechanics from 3D+t TEE images, Med Image Anal 20(1) (2015) 162-72.

[10] W.D. Merryman, F.J. Schoen, Mechanisms of calcification in aortic valve disease: role of mechanokinetics and mechanodynamics, Curr Cardiol Rep 15(5) (2013) 355.

[11] J.A. Leopold, Cellular mechanisms of aortic valve calcification, Circulation. Cardiovascular interventions 5(4) (2012) 605-14.

[12] D. Skowasch, M. Steinmetz, G. Nickenig, G. Bauriedel, Is the degeneration of aortic valve bioprostheses similar to that of native aortic valves? Insights into valvular pathology, Expert Rev Med Devices 3(4) (2006) 453-62.

[13] A. Kostyunin, R. Mukhamadiyarov, T. Glushkova, L. Bogdanov, D. Shishkova, N. Osyaev, E. Ovcharenko, A. Kutikhin, Ultrastructural Pathology of Atherosclerosis, Calcific Aortic Valve Disease, and Bioprosthetic Heart Valve Degeneration: Commonalities and Differences, Int J Mol Sci 21(20) (2020).

[14] C. Dittfeld, A. Mieting, C. Welzel, A. Jannasch, K. Matschke, S.M. Tugtekin, G. Steiner, Molecular Spectroscopic Imaging Offers a Systematic Assessment of Pathological Aortic Valve and Prosthesis Tissue in Biomineralization, Crystals 10(9) (2020).

[15] N. Vyavahare, D. Hirsch, E. Lerner, J.Z. Baskin, F.J. Schoen, R. Bianco, H.S. Kruth, R. Zand, R.J. Levy, Prevention of bioprosthetic heart valve calcification by ethanol preincubation. Efficacy and mechanisms, Circulation 95(2) (1997) 479-88.

[16] M.N. Girardot, M. Torrianni, D. Dillehay, J.M. Girardot, Role of glutaraldehyde in calcification of porcine heart valves: comparing cusp and wall, J Biomed Mater Res 29(7) (1995) 793-801.

[17] P. Human, P. Zilla, Characterization of the immune response to valve bioprostheses and its role in primary tissue failure, The Annals of Thoracic Surgery 71(5) (2001) S385-S388.

[18] D. Bezuidenhout, A. Oosthuysen, P. Human, C. Weissenstein, P. Zilla, The effects of cross-link density and chemistry on the calcification potential of diamine-extended glutaraldehyde-fixed bioprosthetic heart-valve materials, Biotechnol Appl Biochem 54(3) (2009) 133-40.

[19] P. Human, C. Ofoegbu, H. Ilsley, D. Bezuidenhout, J. de Villiers, D.F. Williams, P. Zilla, Decellularization and engineered crosslinking: a promising dual approach towards bioprosthetic heart valve longevity, Eur J Cardiothorac Surg 58(6) (2020) 1192-1200.

[20] A. Neumann, S. Sarikouch, T. Breymann, S. Cebotari, D. Boethig, A. Horke, P. Beerbaum, M. Westhoff-Bleck, H. Bertram, M. Ono, I. Tudorache, A. Haverich, G. Beutel, Early systemic cellular immune response in children and young adults receiving decellularized fresh allografts for pulmonary valve replacement, Tissue engineering. Part A 20(5-6) (2014) 1003-11.

[21] A.E. Kostyunin, A.E. Yuzhalin, M.A. Rezvova, E.A. Ovcharenko, T.V. Glushkova, A.G. Kutikhin, Degeneration of Bioprosthetic Heart Valves: Update 2020, Journal of the American Heart Association 9(19) (2020) e018506.

[22] M.J. Thubrikar, J.D. Deck, J. Aouad, S.P. Nolan, Role of mechanical stress in calcification of aortic bioprosthetic valves, J Thorac Cardiovasc Surg 86(1) (1983) 115-25.

[23] H. Kim, J. Lu, M.S. Sacks, K.B. Chandran, Dynamic Simulation of Bioprosthetic Heart Valves Using a Stress Resultant Shell Model, Annals of Biomedical Engineering 36(2) (2008) 262-275.

[24] M. Toma, S. Singh-Gryzbon, E. Frankini, Z.A. Wei, A.P. Yoganathan, Clinical Impact of Computational Heart Valve Models, Materials (Basel) 15(9) (2022).

[25] D.T. Simionescu, Prevention of calcification in bioprosthetic heart valves: challenges and perspectives, Expert Opin Biol Ther 4(12) (2004) 1971-85.

[26] S. Bertazzo, E. Gentleman, K.L. Cloyd, A.H. Chester, M.H. Yacoub, M.M. Stevens, Nano-analytical electron microscopy reveals fundamental insights into human cardiovascular tissue calcification, Nature Materials 12(6) (2013) 576-583.

[27] V. Cottignoli, M. Relucenti, G. Agrosì, E. Cavarretta, G. Familiari, L. Salvador, A. Maras, Biological Niches within Human Calcified Aortic Valves: Towards Understanding of the Pathological Biomineralization Process, BioMed Research International 2015 (2015) 542687.

[28] C. Delogne, P.V. Lawford, S.M. Habesch, V.A. Carolan, Characterization of the calcification of cardiac valve bioprostheses by environmental scanning electron microscopy and vibrational spectroscopy, J Microsc 228(Pt 1) (2007) 62-77.

[29] O. Bunk, M. Bech, T.H. Jensen, R. Feidenhans'l, T. Binderup, A. Menzel, F. Pfeiffer, Multimodal x-ray scatter imaging, New Journal of Physics 11(12) (2009).

[30] C.S. Peskin, The immersed boundary method, Acta Numerica 11 (2003) 479-517.

[31] R. Henniger, D. Obrist, L. Kleiser, High-order accurate solution of the incompressible Navier–Stokes equations on massively parallel computers, Journal of Computational Physics 229(10) (2010) 3543-3572.

[32] C.J. Permann, D.R. Gaston, D. Andrš, R.W. Carlsen, F. Kong, A.D. Lindsay, J.M. Miller, J.W. Peterson, A.E. Slaughter, R.H. Stogner, R.C. Martineau, MOOSE: Enabling massively parallel multiphysics simulation, SoftwareX 11 (2020).

[33] B.B. Maria Giuseppina Chiara Nestola, Hadi Zolfaghari, Patrick Zulian, Dario De Marinis, Rolf Krause, Dominik Obrist, An immersed boundary method for fluid-structure interaction based on overlapping domain decomposition, arXiv pre-print server (2018).

[34] G.A. Holzapfel, T.C. Gasser, R.W. Ogden, A New Constitutive Framework for Arterial Wall Mechanics and a Comparative Study of Material Models, Journal of elasticity and the physical science of solids 61(1) (2000) 1-48.

[35] F. Auricchio, M. Conti, A. Ferrara, S. Morganti, A. Reali, Patient-specific simulation of a stentless aortic valve implant: the impact of fibres on leaflet performance, Comput Methods Biomech Biomed Engin 17(3) (2014) 277-85.

[36] B. Becsek, L. Pietrasanta, D. Obrist, Turbulent Systolic Flow Downstream of a Bioprosthetic Aortic Valve: Velocity Spectra, Wall Shear Stresses, and Turbulent Dissipation Rates, Front Physiol 11 (2020) 577188.

[37] J.S.E. Corso P., Vennemann B., Obrist D., Leafet futtering and turbulent systolic blood flow after bioprosthetic heart valves, CMBBE { International Symposium on

Computer Methods in Biomechanics and Biomedical Engineering, 2021.

[38] A. Candreva, M. Pagnoni, M.L. Rizzini, T. Mizukami, E. Gallinoro, V. Mazzi, D. Gallo, D. Meier, T. Shinke, J.P. Aben, S. Nagumo, J. Sonck, D. Munhoz, S. Fournier, E. Barbato, W. Heggermont, S. Cook, C. Chiastra, U. Morbiducci, B. De Bruyne, O. Muller, C. Collet, Risk of myocardial infarction based on endothelial shear stress analysis using coronary angiography, Atherosclerosis (2021).

[39] Z. Chen, H. Yu, Y. Shi, M. Zhu, Y. Wang, X. Hu, Y. Zhang, Y. Chang, M. Xu, W. Gao, Vascular Remodelling Relates to an Elevated Oscillatory Shear Index and Relative Residence Time in Spontaneously Hypertensive Rats, Sci Rep 7(1) (2017) 2007.

[40] P. Corso, J. Walheim, H. Dillinger, G. Giannakopoulos, U. Gulan, C.E. Frouzakis, S. Kozerke, M. Holzner, Toward an accurate estimation of wall shear stress from 4D flow magnetic resonance downstream of a severe stenosis, Magn Reson Med 86(3) (2021) 1531-1543.

[41] C. Hahn, M.A. Schwartz, Mechanotransduction in vascular physiology and atherogenesis, Nat Rev Mol Cell Biol 10(1) (2009) 53-62.

[42] V. Mazzi, D. Gallo, K. Calo, M. Najafi, M.O. Khan, G. De Nisco, D.A. Steinman, U. Morbiducci, A Eulerian method to analyze wall shear stress fixed points and manifolds in cardiovascular flows, Biomech Model Mechanobiol 19(5) (2020) 1403-1423.

[43] P. Corso, G. Giannakopoulos, U. Gulan, C.E. Frouzakis, M. Holzner, A Novel Estimation Approach of Pressure Gradient and Haemodynamic Stresses as Indicators of Pathological Aortic Flow Using Subvoxel Modelling, IEEE Trans Biomed Eng 68(3) (2021) 980-991.

[44] M.D. Shoulders, R.T. Raines, Collagen structure and stability, Annu Rev Biochem 78 (2009) 929-58.

[45] C.G. Fuentes-Corona, J. Licea-Rodriguez, R. Younger, R. Rangel-Rojo, E.O. Potma, I. Rocha-Mendoza, Second harmonic generation signal from type I collagen fibers grown in vitro, Biomed Opt Express 10(12) (2019) 6449-6461.

[46] I. Perrotta, M. Davoli, Collagen Mineralization in Human Aortic Valve Stenosis: A Field Emission Scanning Electron Microscopy and Energy Dispersive Spectroscopy Analysis, Ultrastructural Pathology 38(4) (2014) 281-284.

[47] O. Gourgas, K. Khan, A. Schwertani, M. Cerruti, Differences in mineral composition and morphology between men and women in aortic valve calcification, Acta Biomaterialia 106 (2020) 342-350.

[48] G.R. Barnhart, M. Jones, T. Ishihara, A.M. Chavez, D.M. Rose, V.J. Ferrans, Bioprosthetic valvular failure. Clinical and pathological observations in an experimental animal model, J Thorac Cardiovasc Surg 83(4) (1982) 618-31.

[49] A. Whelan, E. Williams, E. Fitzpatrick, B.P. Murphy, P.S. Gunning, D. O'Reilly, C. Lally, Collagen fibre-mediated mechanical damage increases calcification of bovine pericardium for use in bioprosthetic heart valves, Acta Biomater 128 (2021) 384-392.

[50] A. Bakhshian Nik, J.D. Hutcheson, E. Aikawa, Extracellular Vesicles As Mediators of Cardiovascular Calcification, Front Cardiovasc Med 4 (2017) 78.

[51] A.G. Kutikhin, L. Feenstra, A.E. Kostyunin, A.E. Yuzhalin, J.L. Hillebrands, G. Krenning, Calciprotein Particles: Balancing Mineral Homeostasis and Vascular Pathology, Arterioscler Thromb Vasc Biol 41(5) (2021) 1607-1624.

[52] J.D. Hutcheson, M.C. Blaser, E. Aikawa, Giving Calcification Its Due: Recognition of a Diverse Disease: A First Attempt to Standardize the Field, Circ Res 120(2) (2017) 270-273.

[53] A.E. Kostyunin, A.E. Yuzhalin, E.A. Ovcharenko, A.G. Kutikhin, Development of calcific aortic valve disease: Do we know enough for new clinical trials?, Journal of Molecular and Cellular Cardiology 132 (2019) 189-209.

[54] E. Tsolaki, W. Doran, J. Overbeck, L. Magnani, A. Olivo, I.K. Herrmann, S. Bertazzo, Nano-analytical Characterization of Breast Tissue Biopsies Reveals an Association between Spherical Nano and Micro Particles and Invasive Malignant Breast Tumours, bioRxiv (2021) 2020.04.29.067660.

[55] A.C.S. Tan, M.G. Pilgrim, S. Fearn, S. Bertazzo, E. Tsolaki, A.P. Morrell, M. Li, J.D. Messinger, R. Dolz-Marco, J. Lei, M.G. Nittala, S.R. Sadda, I. Lengyel, K.B. Freund, C.A. Curcio, Calcified nodules in retinal drusen are associated with disease progression in age-related macular degeneration, Science translational medicine 10(466) (2018) eaat4544.

[56] M.G. Pilgrim, S. Marouf, S. Fearn, L. Csincsik, E. Kortvely, J.C. Knowles, G. Malek, R.B. Thompson, I. Lengyel, Characterization of Calcium Phosphate Spherical Particles in the Subretinal Pigment Epithelium–Basal Lamina Space in Aged Human Eyes, Ophthalmology Science 1(3) (2021).

[57] A.H.C. Anthis, E. Tsolaki, L. Didierlaurent, S. Staubli, R. Zboray, A. Neels, D. Dietrich, P. Manser, L.M. Desbiolles, S. Leschka, S. Wildermuth, S. Lehner, P. Chavatte-Palmer, W. Jochum, P. Wick, A. Dommann, T. Bürki-Turnherr, T. Fischer, R. Hornung, S. Bertazzo, I.K. Herrmann, Nano-analytical characterization of endogenous minerals in healthy placental tissue: mineral distribution, composition and ultrastructure, Analyst 144(23) (2019) 6850-6857.

[58] D.T. Grubb, W.J. Kennedy, H. Koerner, N.S. Murthy, Simulation of SAXS patterns from oriented lamellar structures and their elliptical trajectories, Polymer 220 (2021).

[59] L. Ge, F. Sotiropoulos, Direction and magnitude of blood flow shear stresses on the leaflets of aortic valves: is there a link with valve calcification?, J Biomech Eng 132(1) (2010) 014505.

[60] A. Arzani, S.C. Shadden, Wall shear stress fixed points in cardiovascular fluid mechanics, Journal of biomechanics 73 (2018) 145-152.

[61] U. Morbiducci, V. Mazzi, M. Domanin, G. De Nisco, C. Vergara, D.A. Steinman, D. Gallo, Wall shear stress topological skeleton independently predicts long-term restenosis after carotid bifurcation endarterectomy, Annals of biomedical engineering 48 (2020) 2936-2949.

[62] P.C. Corso, Fegal; Nestola, Maria; Jahren, Silje; Obrist, Dominik, Study Of The Flutter Kinematics And Blood Flow Motion For Bioprosthetic Aortic Valves With Different Designs, 2022 HVS Annual Meeting, 2022.

[63] V.J. Ferrans, S.W. Boyce, M.E. Billingham, M. Jones, T. Ishihara, W.C. Roberts, Calcific deposits in porcine bioprostheses: Structure and pathogenesis, The American Journal of Cardiology 46(5) (1980) 721-734.

[64] F.J. Schoen, R.J. Levy, Tissue heart valves: Current challenges and future research perspectives, 47(4) (1999) 439-465.

[65] F.J. Schoen, J.W. Tsao, R.J. Levy, Calcification of bovine pericardium used in cardiac valve bioprostheses. Implications for the mechanisms of bioprosthetic tissue mineralization, Am J Pathol 123(1) (1986) 134-45.

[66] E. Jorge-Herrero, J.M. Garcia Paez, J.L. Del Castillo-Olivares Ramos, Tissue heart valve mineralization: Review of calcification mechanisms and strategies for prevention, Journal of applied biomaterials & biomechanics : JABB 3(2) (2005) 67-82.

[67] M.J. Thubrikar, J. Aouad, S.P. Nolan, Patterns of calcific deposits in operatively excised stenotic or purely regurgitant aortic valves and their relation to mechanical stress, The American Journal of Cardiology 58(3) (1986) 304-308.

[68] A.J. Dalgliesh, M. Parvizi, C. Noble, L.G. Griffiths, Effect of cyclic deformation on xenogeneic heart valve biomaterials, PLoS One 14(6) (2019) e0214656.

[69]. Salman HE, Saltik L, Yalcin HC, Computational Analysis of Wall Shear Stress Patterns on Calcified and Bicuspid Aortic Valves: Focus on Radial and Coaptation Patterns, Fluids. 2021;6(8).

[70]. Hasler D, Obrist D, Three-dimensional flow structures past a bio-prosthetic valve in an in-vitro model of the aortic root, PLoS One. 2018;13(3).

71. Cao K, Sucosky P, Computational comparison of regional stress and deformation characteristics in tricuspid and bicuspid aortic valve leaflets, Int. J. Numer. Meth. Biomed. Engng., 2017;33(3).

[72].   Mattor N, Williams TJ, Hewett DW, Algorithm for solving tridiagonal matrix problems in parallel, Parallel Comput. 1995;21:1769–1782.

[73].   Krause R, Zulian P, A Parallel Approach to the Variational Transfer of Discrete Fields between Arbitrarily Distributed Unstructured Finite Element Meshes, SIAM Journal on Scientific Computing 2016; 38(3).

[74].   Balay S., Abhyankar S, Adams MF, Benson S, Brown J, Brune P, Buschelman K, Constantinescu EM, Dalcin L, Dener A, Eijkhout V, Faibussowitsch J, Gropp WD, Hapla V, Isaac T, Jolivet P, Karpeev D, Kaushik D, Knepley MG, Kong F, Kruger S, May DA, Curfman McInnes L, Tran Mills T, Mitchell L, Munson T, Roman JE, Rupp K, Sanan P, Sarich J, Smith BF, Zampini S, Zhang H, Zhang J, PETSc Web page, https://petsc.org/ 2023.

Graphical Abstract
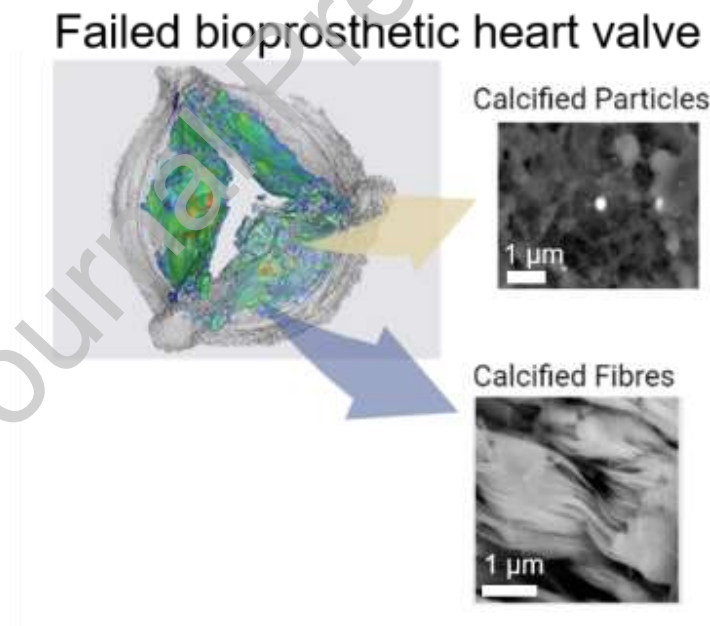
Statement of significance

Bioprosthetic valve calcification is a well-known clinically significant phenomenon, leading to valve failure. The nanoanalytical characterisation of bioprosthetic valves gives insights into the highly abundant, extensive calcification and disorganization of the collagen network and the presence of calcium phosphate particles previously reported in native cardiovascular tissues. While the collagen matrix mineralisation can be primarily attributed to a combination of chemical and mechanical alterations, the calcified particles are likely of host cellular origin. This work presents a straightforward route to mineral identification and characterization at high resolution and sensitivity, and with full histoanatomical context, hence providing design cues for improved bioprosthetic valve alternatives.

Declaration of interests

☒ The authors declare that they have no known competing financial interests or personal relationships that could have appeared to influence the work reported in this paper.

☐ The authors declare the following financial interests/personal relationships which may be considered as potential competing interests: